Eur. Phys. J. D **22**, 163–182 (2003)
DOI: 10.1140/epjd/e2003-00012-2

THE EUROPEAN PHYSICAL JOURNAL D

Double Penning trap technique for precise g factor determinations in highly charged ions

H. Häffner[1,2,a], T. Beier[1], S. Djekić[2], N. Hermanspahn[2,b], H.-J. Kluge[1], W. Quint[1], S. Stahl[1,2], J. Verdú[2], T. Valenzuela[2], and G. Werth[2,c]

[1] GSI, Atomic Physics, Planckstr. 1, 64291 Darmstadt, Germany
[2] Institut für Physik, Universität Mainz, 55099 Mainz, Germany

Received 17 June 2002 / Received in final form 13 September 2002
Published online 21 January 2003 –

Abstract. We present a detailed description of an experiment to determine the magnetic moment of an electron bound in hydrogen-like carbon. This forms a high-accuracy test of bound-state quantum electrodynamics. Special emphasis is given to the discussion of systematic uncertainties which limit our present accuracy. The described experimental setup may also be used for the determination of g factors in other highly charged ions.

PACS. 32.10.Dk Electric and magnetic moments, polarizability – 06.20.Jr Determination of fundamental constants – 31.30.Jv Relativistic and quantum electrodynamic effects in atoms and molecules

1 Introduction

1.1 General

The experimental determination of the magnetic moment (g_J factor) of the bound electron in hydrogen-like ions is an important test of Quantum Electrodynamics (QED) in strong Coulomb fields [1–3]. It represents a rather clean test of pure QED effects because it is not very sensitive to nuclear structure effects which usually are more difficult to take into account [4–6]. Precise experimental data on the g_J factor of the bound electron in hydrogenic systems have been available until recently only for the hydrogen atom ([7–9] and references therein) and the $^4He^+$-ion [10]. These results, however, were not sensitive to bound-state QED effects, which are very small at low values of the nuclear charge Z. In addition to these measurements, the magnetic moments of the electrons bound to $^{207}Pb^{81+}$ and $^{209}Bi^{82+}$-nuclei were extracted from lifetime measurements of the excited hyperfine splitting level of the ground state to a precision of about 10^{-3} [11–13] which is not sufficient to observe bound-state QED effects.

Recently we have published the result of an experiment on the g_J factor of hydrogen-like $^{12}C^{5+}$ using a single ion confined in a Penning ion trap [3]. The precision of a few parts in 10^9 was sufficient to test bound-state QED corrections of order α/π on the 1% level in spite of the rather low value of Z. It was even possible to derive a new value for the mass of the electron [14,15] which is more precise than the current accepted value [16]. An extension of our method to hydrogen-like or lithium-like ions with higher Z values would investigate the bound-state QED contributions even more stringently. In this article we give a detailed description of our experiment with special emphasis of the possible systematic effects which at present limit our precision.

The paper is organized as follows: after a short introduction on the measurement principle, we describe the experimental set-up and the basic techniques used for the experiments (Sect. 2). Section 3 describes measurements of the ion's motional frequencies and the detection of induced spin transitions. Section 4 is devoted to a discussion of the systematic uncertainties.

2 Experimental techniques

2.1 Measurement principle

The g_J factor of an electron is defined in terms of the ratio of its magnetic moment $\boldsymbol{\mu}$ to its angular momentum $\mathbf{J}$

$$\boldsymbol{\mu} = -g_J \frac{e}{2m_e}\mathbf{J}, \tag{1}$$

[a] *Present address*: Institut für Experimentalphysik, Universität Innsbruck, 6020 Innsbruck, Austria.
[b] *Present address*: 54 Warrington St., St. Albans, Christchurch 8001, New Zealand.
[c] e-mail: `werth@uni-mainz.de`

where e is the (positive) charge of the electron and m_e its mass. The energy difference ΔE between the two orientations of the electron spin in a magnetic field $\mathbf{B} = B_z \mathbf{e}_z$ is

$$\Delta E = -\boldsymbol{\mu} \cdot \mathbf{B} = g_J \frac{e\hbar}{2m_e} B_z. \quad (2)$$

Introducing the cyclotron frequency $\omega_c^e = (e/m_e) \times B_z$ and the Larmor precession frequency $\omega_L = \Delta E/\hbar$ of the electron, the g_J factor can be written as

$$g_J = 2\frac{\omega_L}{\omega_c^e} \cdot \quad (3)$$

Thus the g_J factor of the electron can be determined from a measurement of the Larmor precession frequency and the cyclotron frequency of the electron.

In our case the electron is bound to a nucleus and therefore its cyclotron frequency is not directly accessible. One solution would be to store a free electron and measure the cyclotron frequency separately. This would, however, have some drawbacks due to the opposite charge of the electron compared to the ion: the ion and the electron cannot be stored at the same time in the same trap and the measurement of the two frequencies requires a change in the trapping voltage (*e.g.* [17]). Contact potentials, patch effects, and defects in the metal lattice of the trap material might result in different positions of the potential energy minima for the ion and the electron, and the two particles would be located at different regions in the trap. If the magnetic field is not perfectly homogeneous this then leads to a different field strength experienced by the ion and the electron.

To avoid these complications we instead measure the cyclotron frequency ω_c of the ion. Inserting ω_c in equation (3) yields

$$g_J = 2\frac{\omega_L}{\omega_c}\frac{\omega_c}{\omega_c^e} \cdot \quad (4)$$

ω_c/ω_c^e in the same magnetic field is directly related to the mass ratio of the two particles. For $^{12}C^{5+}$ it was obtained from a measurement on carbon ions at the University of Washington [17,18] with a Penning-trap mass spectrometer on which the current CODATA value for the electron mass is based [16]. Together with the binding energies also taken from [16] we get

$$\omega_c(^{12}C^{5+})/\omega_c^e = 0.000\,228\,627\,210\,33\,(50). \quad (5)$$

Equation (4) shows that to measure the g_J factor of the bound electron only the frequency ratio ω_L/ω_c has to be determined.

2.2 Our setup

As described in [19,20], our experiments are performed on a single hydrogen-like ion confined in a Penning trap with a strong magnetic field (B = 3.8 T) (Fig. 1). The trap consists of a stack of cylindrical electrodes with an

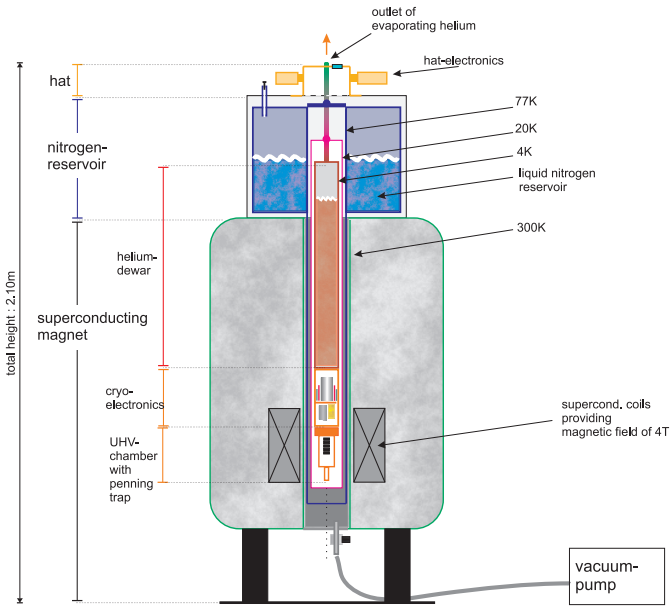

Fig. 1. Experimental setup.

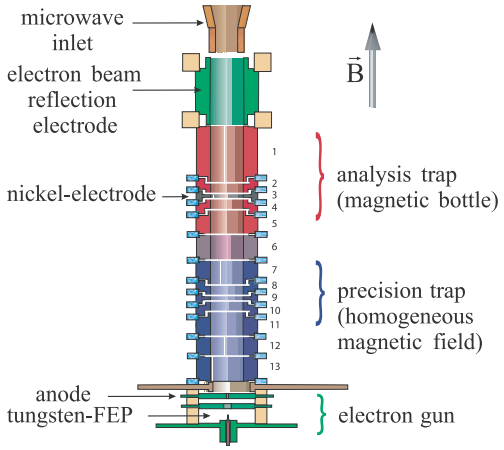

Fig. 2. Sketch of the trap electrodes.

inner diameter of 7 mm (Fig. 2, Tab. 1). Following a proposal by Gabrielse *et al.* [21], 5 electrodes form one trap: between one ring electrode and two symmetrically placed endcap electrodes we have two correction electrodes. We apply a negative voltage of typically 2–10 volts to the ring electrodes while the endcaps are held at ground potential. Thus for positively charged ions a potential minimum of a few eV depth along the trap axis (z axis) is formed. A voltage applied to the correction electrodes serves to modify the shape of the trapping potential. Choosing a ratio of 0.877 [21] between the voltages applied to the correction electrodes and to the ring electrodes, we obtain a fairly harmonic quadrupole trapping potential near the center of the ring electrode. Fine tuning of the correction voltage, as described later, minimizes non-harmonic contributions to the potential.

Table 1. Electrode dimensions. All the electrodes have an inner diameter of 7 mm.

Electrode number (see Fig. 2)	Length [mm]
1	9.34
2	2.75
3	0.92
4	2.75
5	4.60
6	5.06
7	4.83
8	2.75
9	0.92
10	2.75
11	4.83
12	3.68
13	5.06

As seen in Figure 2, we have two traps of identical geometry spaced by a 1 cm long separation electrode. The difference between the two traps is that the ring electrode of the upper trap is made from nickel while all other electrodes are oxygen-free (OFHC) copper. The whole device is gold coated to avoid surface charges. The nickel ring introduces an inhomogeneity in the trap's magnetic field, needed to analyze the spin direction of the stored ion (Sect. 3.2). Therefore we call the corresponding trap the "analysis trap". We term the trap with the homogeneous magnetic field the "precision trap". At the lower end of the stack of electrodes we have a field emission cathode. Emitted electrons are accelerated to a few hundred electron volts, pass through the trap arrangement and are reflected by an additional electrode at the upper end. Coulomb interactions between the electrons cause the beam to expand and to hit a pellet near the field emission cathode. Depending on the electron energy, ions of the pellet material as well as impurities at different charge states are released from the surface, drawn into the electron beam and ionized further. Some of them are confined in the precision trap. In order to achieve long storage times it is essential to operate the trap in extremely high vacuum since the main loss mechanism is charge exchange with a neutral particle. The trap's housing is kept in thermal contact with a liquid helium reservoir. Cryopumping removes essentially all background molecules. From extended measurements on a cloud of stored $^{12}C^{5+}$ ions we found that the storage time is longer than one year. We derive that the residual pressure in the trap's container is below 10^{-16} mbar. This assumes a value of $\sigma = 1.35 \times 10^{-14}$ cm^2 for the C^{5+} to He charge exchange cross-section [22].

Our magnetic field is provided by a standard superconducting NMR magnet from Oxford Instruments. It has a vertically oriented room temperature bore into which the apparatus is inserted. The apparatus is shown in Figure 1. It consists of two Dewar vessels, electronics and the vacuum chamber containing the trap. Liquid helium cools the apparatus down to 4 K. Electronic circuits [23] for ion detection are placed within 20 cm of the traps to avoid parasitic capacitances of the cables. They consist mainly out of three high-Q-r.f. amplifiers for ion detection.

2.3 Frequencies in an ideal and a physical Penning trap

The motion of a single ion in the Penning trap is well understood (*e.g.* [24]). The solution of the equation of motion in an ideal quadrupole potential and a superposed homogeneous magnetic field yields three harmonic oscillations with frequencies

$$\omega_+ = \frac{\omega_c}{2} + \sqrt{\frac{{\omega_c}^2}{4} - \frac{{\omega_z}^2}{2}} \tag{6}$$

$$\omega_- = \frac{\omega_c}{2} - \sqrt{\frac{{\omega_c}^2}{4} - \frac{{\omega_z}^2}{2}} \tag{7}$$

$$\omega_z = \sqrt{\frac{eU}{md^2}}, \tag{8}$$

where U is the applied voltage, d the characteristic trap dimension (defined by $d = \sqrt{\frac{1}{2}({z_0}^2 + \frac{{\rho_0}^2}{2})}$ where $2z_0$ is the distance between the two endcaps and ρ_0 is the ring radius [21]) and ω_c the ion's cyclotron frequency. ω_+, ω_z, ω_- refer to the perturbed cyclotron, axial, and magnetron oscillations, respectively. For the case of $^{12}C^{5+}$ in a field of 3.8 T, $U \approx 13$ V and $d = 3$ mm, we have $\omega_+ \approx 2\pi \times 24$ MHz, $\omega_z \approx 2\pi \times 1$ MHz, $\omega_- \approx 2\pi \times 20$ kHz. The unperturbed cyclotron frequency ω_c is not an eigenfrequency of the ion motion, but the ratio ω_L/ω_c is required to determine the g factor (*cf.* Eq. (4)).

There are several ways to derive ω_c from measured frequencies. We choose the so-called invariance theorem [24,25]

$${\omega_c}^2 = {\omega_+}^2 + {\omega_z}^2 + {\omega_-}^2 , \tag{9}$$

because it is rather insensitive to trap imperfections, such as an ellipticity of the trap or a tilt of the trap with respect to the magnetic field.

The eigenfrequencies of an ion in a non-ideal trap potential are shifted compared to the values given in equations (6–8). These shifts have been calculated by several authors [24,36–38]. The perturbations arise from a slightly inhomogeneous magnetic field, anharmonicities in the electrostatic potential and a small tilt between the trap axis and the magnetic field direction.

The axially symmetric potential $\Phi(z, r)$ can be written as a series expansion in Legendre polynomials P_l

$$\Phi(z, r) = \sum_{l=0}^{\infty} C_l \left(\frac{r}{d}\right)^l P_l \left(\frac{z}{\sqrt{r^2 + z^2}}\right) \cdot \tag{10}$$

The leading term is a quadrupole potential ($l = 2$) which depends quadratically on the coordinates. Odd terms in the expansion are very small because of the mirror symmetry of the device with respect to the center plane. In addition, the length of the electrodes is chosen such that the octupole (C_4) and dodecapole (C_6) contributions to

the trapping potential are simultaneously minimized [21]. For the remaining frequency shifts we consider only the octupole term

$$\Delta V = V_0 C_4 \frac{z^4 - 2z^2r^2 + \frac{3}{8}r^4}{2d^4} \cdot \tag{11}$$

Similarly the magnetic field can be expanded. For our purposes it is sufficient to take only a quadratic component in the magnetic field (*magnetic bottle*) into account

$$\Delta \mathbf{B} = B_2 \left[(z^2 - r^2/2)\mathbf{e}_z - z\mathbf{r}\right]. \tag{12}$$

The change in the magnetron motion is very small and can be neglected. Then we consider only the axial and perturbed cyclotron motions. The shift $\Delta\omega_z$ of the axial frequency is given by [24]

$$\frac{\Delta\omega_z}{\omega_z} = \frac{3}{2}\frac{C_4}{C_2}\frac{1}{E_{\max}} E_z + \frac{1}{m\omega_z^2}\frac{B_2}{B_0} E_+, \tag{13}$$

E_z is the total energy in the axial motion, E_+ the corresponding value in the cyclotron motion. $E_{\max}$ denotes axial well depth. For constant axial energy, we obtain a linear dependence of the axial frequency on the cyclotron energy

$$E_+ = m\omega_z \frac{B_0}{B_2} \Delta\omega_z. \tag{14}$$

This relation is used in our experiment to obtain values for the cyclotron energies from measurements of axial frequencies.

For the perturbed cyclotron frequency ω_+, we get

$$\frac{\Delta\omega_+}{\omega_+} = -\frac{1}{m\omega_+^2}\frac{B_2}{B_0} E_+ + \frac{1}{m\omega_z^2}\frac{B_2}{B_0} E_z. \tag{15}$$

This shift arises from variations in the magnetic field in the different space regions encountered by the ion at different energies. Finally the Larmor-precession frequency is affected by the magnetic field's inhomogeneity

$$\frac{\Delta\omega_{\mathrm{L}}}{\omega_{\mathrm{L}}} = -\frac{1}{m\omega_+^2}\frac{B_2}{B_0} E_+ + \frac{1}{m\omega_z^2}\frac{B_2}{B_0} E_z. \tag{16}$$

2.4 Axial detection

Oscillating ions induce image charges in the trap electrodes. For the axial motion, this leads to an oscillating current $I = \mathrm{d}Q/\mathrm{d}t = (q/d)\dot{z}$ between the trap electrodes, where q is the charge of the ion and $\dot{z}$ its velocity. We connect one of the correction electrodes to a resonant circuit, while all other electrodes are at a.c. ground potential. Resonant circuits are placed very close to the trap and held at liquid helium temperature. Each circuit consists of a superconducting coil and the trap electrodes as capacitance. For the analysis trap we achieve a quality factor $Q = 2\,500$ and a corresponding resonance resistance of $R = 20$ MΩ. The parameters for the precision trap are $Q = 1\,000$ and

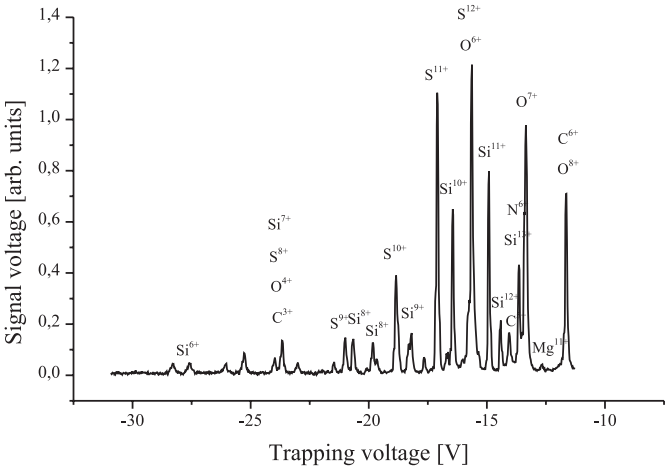

Fig. 3. Axial signals of different ion species stored simultaneously. Various charge states of C, O, S and Si can be identified.

$R = 10$ MΩ. If we tune the trap voltage to such a value that the ions axial frequency coincides with the resonant frequency of the circuit, the induced current leads to a voltage drop across the circuit of a few nV for a single trapped ion. The induced voltage is inductively coupled to a field-effect transistor. To avoid carrier freeze-out at 4 K, we use GaAs transistors. Figure 3 shows axial signals from several ion species and charge states simultaneously present in the trap. They are sequentially brought into resonance with the detection circuit by ramping the trap voltage. For identification of the different species we used equation (8) which allows to calculate the axial frequencies sufficiently accurate. For signals like those shown in Figure 3, the axial ion energy is of the order of an eV.

2.5 Radial detection

As in the case of the axial motion, the ion oscillation in the radial plane at frequency ω_+ induces image charges in the trap electrodes. We use one of the compensation electrodes for detection of ω_+. It is split in two segments which are connected to a resonant circuit. Thus, the induced current can be observed. In contrast to the axial resonance, fine tuning of the ion oscillation frequency with the magnetic field is not possible since the required stability of our magnetic field does not allow any variation. Therefore we choose a modest $Q = 400$ for our circuit at 24 MHz, which is the approximate cyclotron frequency of $^{12}C^{5+}$ in our field of 3.8 tesla. The rather low Q-value makes the frequency setting not too difficult. Furthermore we added several GaAs switching capacities to the circuit to allow changes of the circuit frequency in discrete steps. Figure 4 shows a Fourier transform of the induced current in the radial circuit. It exhibits the signals from 6 $^{12}C^{5+}$ ions. The ions have slightly different frequencies since they are moving in different orbits in the inhomogeneous magnetic field. Ions moving faster (having a larger cyclotron orbit) produce a stronger signal. Typical ion energies in this measurement are about 1 keV. In this case the distance

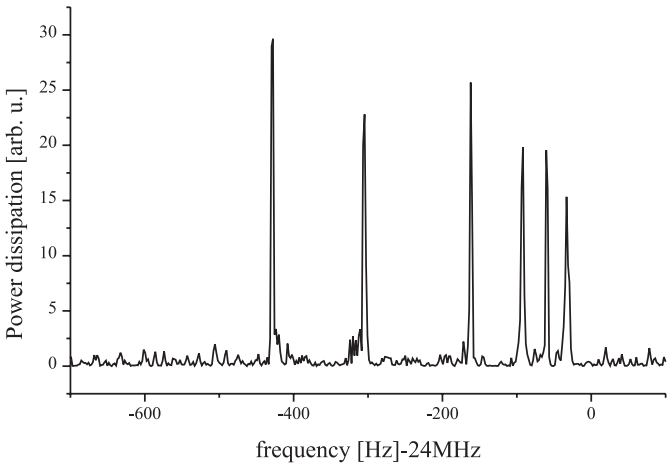

Fig. 4. Fourier transform of the current induced by the cyclotron motion of 6 ions. Due to the magnetic field inhomogeneity, ions of lower cyclotron energy have higher cyclotron frequencies. The ion energies range between 100 eV and 1 keV.

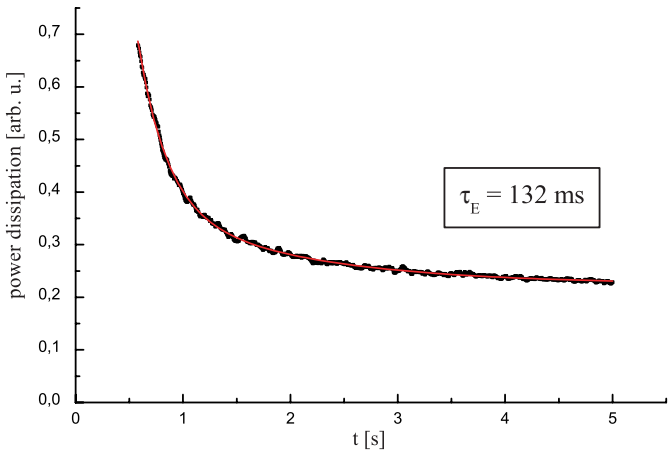

Fig. 5. Resistive cooling of the axial motion of a single ion. The experimentally observed cooling rate of 132 ms is in agreement to the value calculated from [26]. The zero line is given by the noise power with an empty trap.

between two ions is of the order of 0.2 mm and energy exchange between them due to Coulomb interaction can be neglected.

2.6 Single ion preparation

After ion creation by electron bombardment of the target surface, ions of different q/m ratios are simultaneously confined in the trap as shown in Figure 3. Unwanted species are removed by selective excitation of their axial frequency until they hit the trap electrodes and are lost. A reduction in ion number for the species under investigation is performed by carefully lowering the potential depth, while the cyclotron energy of the ions is high ($\sim$ 100 eV). Due to energy transfer from the cyclotron to the axial degree of freedom by Coulomb interaction, ions leave the trap until only one single ion is left. The whole process from creating an ion cloud to the preparation of a single $^{12}C^{5+}$-ion takes less than 5 minutes.

2.7 Ion cooling

2.7.1 Axial cooling

If the ions are continuously kept in resonance with the outer resonant circuit, thermal equilibrium will be established. The high kinetic energy of the ions will be dissipated through the resonant impedance and the ions will acquire the temperature of the environment. The energy evolution for a single ion can be described very well by an exponential $E = E_0 \exp(-\gamma t)$ (Fig. 5)

$$\gamma = \frac{q^2}{m}\frac{R}{d^2}\,. \tag{17}$$

This is because the current induced by the ion's motion is proportional to its velocity and therefore the dissipated power is proportional to the kinetic energy. Deviation from the exponential cooling behaviour occurs when the cooling force is not proportional any more to the kinetic energy of the ions. A possible reason is that the ion frequency depends on the energy and therefore the resistance of the resonant circuit at the ion frequency changes during the cooling process. This is particularly important for the cooling of the axial motion in our cylindrical trap, because for large amplitudes the motion is no longer harmonic since higher order multipole components in the trapping potential become significant. In addition, the situation becomes more complicated in the case of a cloud of ions [26], because only the center-of-mass mode is cooled resistively. The other modes are only cooled due to their coupling to the center-of-mass mode. This is easily understood in the case of the so-called breathing mode, where the center of the charges does not move at all and therefore to first order no current is induced. However, by the Coulomb-interaction (ion-ion collisions) or trap anharmonicities from space charge potentials, energy transfer between the modes occurs. Figure 6 shows the cooling of a cloud of about 30 $^{12}C^{5+}$-ions with an initial mean kinetic energy of about 13 eV in a potential well of 50 eV. Due to the high energy, the axial frequency is shifted downwards by about 5% so that only the cold ions in this ensemble are in resonance with the cooling circuit and are cooled. This results in the initial fast decrease of the total noise power in Figure 6. This time constant is the same as measured for ion clouds with low kinetic energy for which the trap anharmonicity can be neglected. For large times the cooling process is dominated by the energy flow from the non-center-of-mass modes to the center-of-mass mode. We measure a time constant of 5 s after the cloud has settled down.

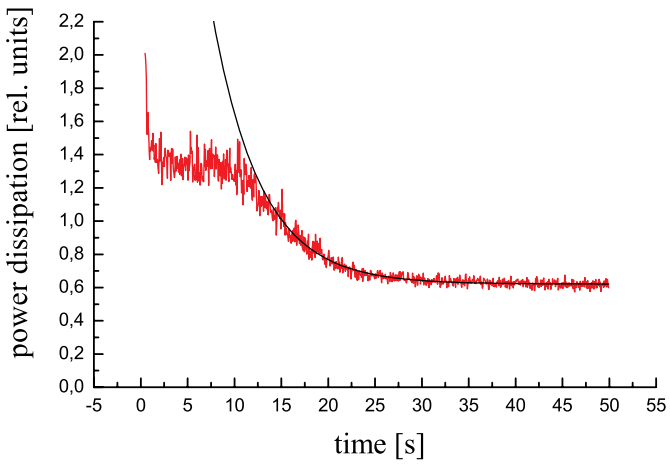

Fig. 6. Resistive cooling of the axial motion of an ion cloud. The time constant of the exponential fit to the tail is 5 s. The zero line is given by the noise power with an empty trap.

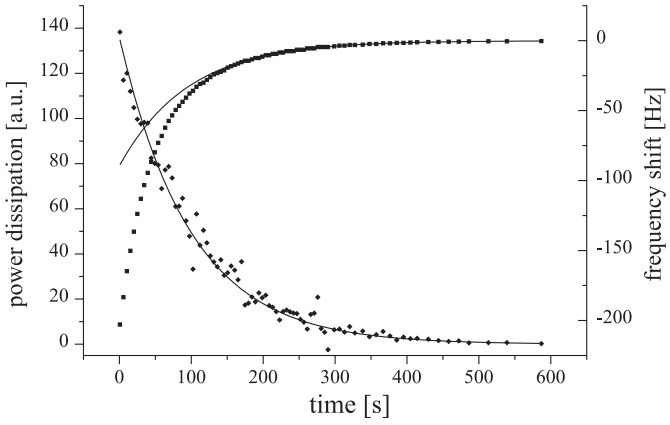

Fig. 7. Resistive cooling of the cyclotron motion of a single ion. While the ion's energy is decreased the cyclotron frequency increases due to the inhomogeneity of the magnetic field. For low ion energies the magnetic field depends on the square of the coordinates (solid line).

2.7.2 Cyclotron cooling

For the cyclotron mode the cooling principle is the same as for the axial mode. The Q-value of the resonant circuit is chosen to be smaller than in the case of the axial circuit and consequently the time constant is larger (100 s). Along with the decrease of the cyclotron energy we observe a shift of the cyclotron frequency with the same time constant (Fig. 7) due to the inhomogeneity of the magnetic field. Fourth and higher order contributions to the magnetic field lead to the deviation from the exponential.

2.7.3 Magnetron cooling

In contrast to the axial and cyclotron mode, reducing the energy of the metastable magnetron mode would lead to an increase of the magnetron orbit and finally to the loss of the ion. Therefore, no resonant circuit at this frequency is attached to the trap. To reduce the magnetron radius we couple the magnetron oscillation to the axial mode by an r.f. field at the sum frequency of both oscillations. This so-called sideband-coupling technique is of great importance for our experiment and we will discuss it in more detail in the following section.

2.8 Sideband coupling and avoided crossing

2.8.1 Sideband coupling

Sideband coupling (see [24,27,28]) relies on the fact that an ion with eigenfrequencies ω_1 and ω_2 can absorb photons with frequencies $\omega_1 \pm \omega_2$. Coupling two modes in a Penning trap by an r.f.-field at the difference frequency $\omega_1 - \omega_2$ leads to a quantum-number exchange between these two modes. The absorption of an r.f.-photon at this frequency results in a loss of one quantum number in one mode and a gain in the other one. Also, stimulated emission can take place, with the opposite result. When one of the motions is cooled resistively coherence is lost and the quantum numbers for both modes tend to equalize. Expressed in terms of the energies E_1 and E_2 we obtain [24]

$$|E_2| = \frac{\omega_2}{\omega_1}|E_1|. \tag{18}$$

If the magnetron motion is involved, the situation is somewhat changed because it has to be described by an inverted harmonic oscillator, introducing a minus sign in the total magnetron energy. Therefore to reduce the magnetron orbit, we have to apply an r.f.-field to one segment of the split correction electrode not at the lower but at the upper axial magnetron sideband $\omega_z + \omega_-$.

2.8.2 Avoided crossing

The absorption of the sideband photons is coherent. If we start with quantum number zero in mode 1, we will arrive in a time given by half of the inverse Rabi frequency Ω at quantum number zero in mode 2, and the initial quantum number of mode 2 in mode 1. Thus the amplitudes of both modes are modulated by $\cos(\Omega t + \phi)$ with a phase-shift of $\Delta\phi = \pi/2$ between the modes. The time evolution of the axial motion can now be written as

$$\begin{aligned} z(t) &= \cos(\Omega t)\sin(\omega_z t) \\ &= \frac{1}{2}\left[\sin\left((\omega_z + \Omega)t\right) + \sin\left((\omega_z - \Omega)t\right)\right]. \end{aligned} \tag{19}$$

Now two components of the axial frequency show up. This is experimentally verified and shown in Figure 8 for r.f.-coupling of the axial and the magnetron mode at the sideband $\omega_z + \omega_-$. The splitting of the two resonances is proportional to the energy exchange rate Ω^{-1} between the two modes. A classical treatment has been given by Cornell *et al.* in reference [27], quantum mechanically it

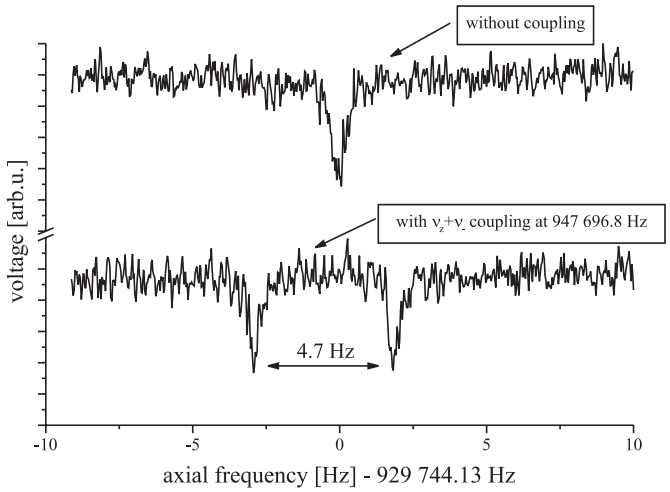

Fig. 8. Fourier spectrum of the axial motion without (upper curve) and with (lower curve) sideband excitation at the frequency $\omega_z + \omega_-$. The splitting of the axial frequency is not symmetric due to a slight detuning of the sideband drive from the resonance (Fig. 9).

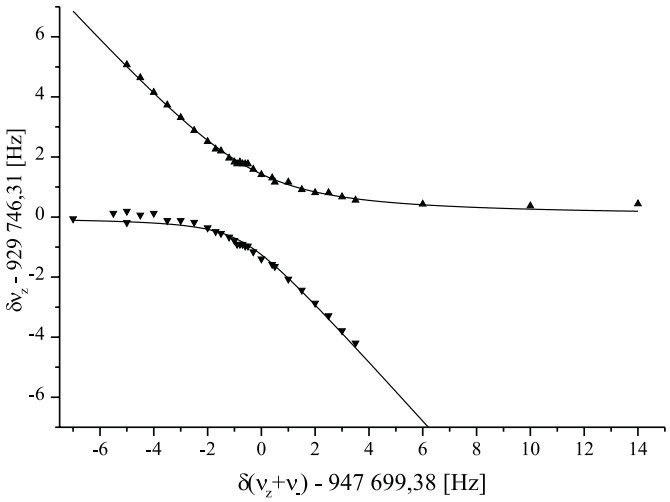

Fig. 9. Avoided crossing of axial frequency due to its coupling to the magnetron mode. The fits are according to equation (20).

has been discussed in [28]. The situation is more complicated if the coupling sideband is detuned by some amount δ. We are not going into the details here but refer to [27]. The position of the two frequency components $\omega + \epsilon_{1,2}$ of one mode is given by [27]

$$\epsilon_{1,2} = -\frac{\delta}{2} \pm \sqrt{\delta^2 + |V|^2}, \tag{20}$$

where V is the amplitude of the coupling-r.f.-field. Figure 9 shows a good agreement of this formula with our measurement.

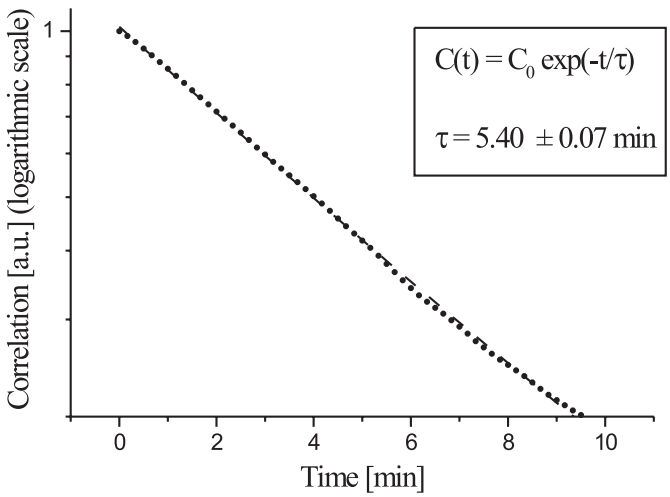

Fig. 10. Autocorrelation of the ion's cyclotron energy. The ion was held in thermal equilibrium at 4.2 K for 2 days.

2.9 Ion temperature

In the ideal case the ion temperature will be equal to the temperature of the environment for all degrees of freedom. However, electronic perturbations may heat the ion. Since our final accuracy in the g_J factor measurement depends on corrections which arise from a finite ion temperature, it is essential to determine experimentally the actual ion temperature in the axial as well as in the radial mode.

To measure the temperature of the cyclotron mode of a single ion, we monitored the axial frequency in the analysis trap over a period of 2 days, performing a measurement every 10 s. The magnetic field inhomogeneity in the analysis trap, caused by the nickel ring electrode, shifts the axial frequency when the cyclotron energy changes due to thermal fluctuations (see the detailed discussion in Sect. 4 and Eq. (14)). The shift amounts to 5 Hz per meV of cyclotron energy as calculated from the measured magnetic field inhomogeneity. When we compile a histogram of the cyclotron energies we obtain an exponential decrease of the probability of a certain energy with increasing energy. The corresponding temperature from a Boltzmann distribution fit gives 4.90 (8) K. The slight disagreement with the expected temperature arises from additional variations of the axial frequency by fluctuations in the trapping voltage which are of the order of a few ppm. A calculation of the autocorrelation function of the energy fluctuation (Fig. 10) gives a time constant in the analysis trap of 5.40 (7) min which is in excellent agreement with the measured cooling time constant of 5.42 (28) min.

A measurement of the axial temperature of a single ion is more difficult. We prepare the ion in the precision trap. The axial energy is brought into equilibrium with the cyclotron energy by coupling the two modes with a r.f-drive at $\omega_+ - \omega_z$ applied to one segment of the split correction electrode for a time of 10 s. This is about a factor of 100 longer than the energy exchange time as derived from the splitting of the two axial dips (see Sect. 2.8.1, *cf.* Fig. 8). This ensures that the two modes have the

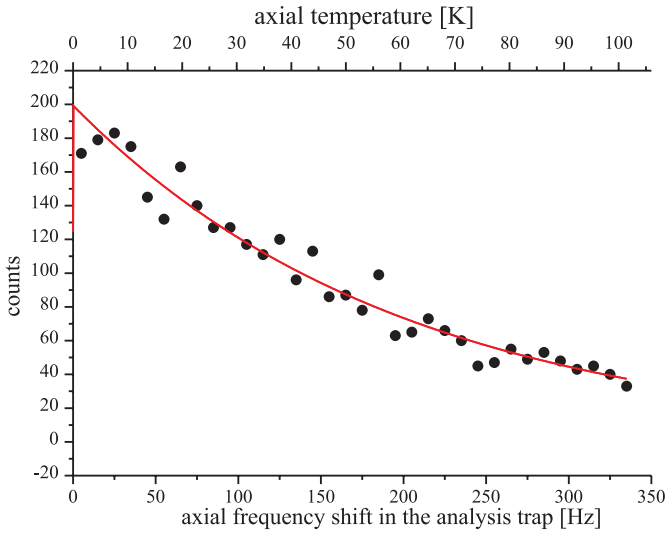

Fig. 11. Measured axial frequencies in the analysis trap after sideband coupling of the axial and cyclotron mode in the precision trap. The measurement yields the ion's axial energy distribution in the precision trap (upper scale). The exponential least-squares fit (solid line) corresponds to a temperature of 61 ± 7 K.

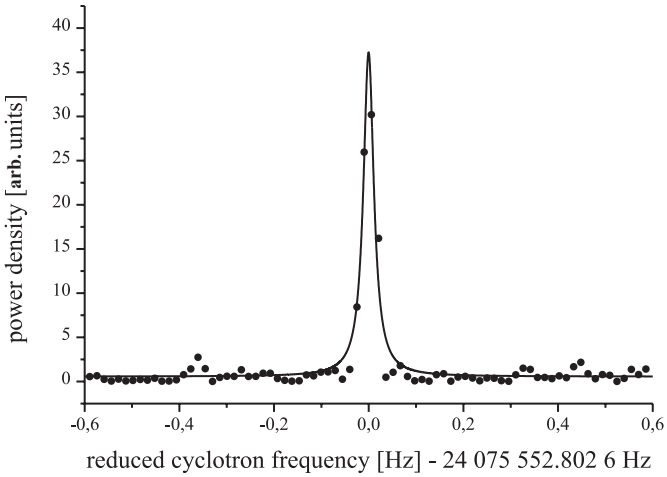

Fig. 12. Fourier transform of the current induced by the cyclotron motion of a single ion. The full line width $\Delta\omega_+/\omega_+$ is 10^{-9}. The ion's cyclotron energy was 2 eV.

same quantum number and we have $E_+ = (\omega_+/\omega_z) \times E_z$ (Eq. (18)). Then the ion is transferred to the analysis trap where the cyclotron energy is determined as described above. Plotting the axial energies, we obtain Figure 11. The measured temperature is 61 (7) K. This is much higher than the ambient temperature of 4.2 K at which the cooling circuit is maintained. This means that in addition to the Johnson noise of our circuit, another noise source is present which has not been identified so far. An assumption that the attached transistor would represent this source of additional noise seems not to be correct when we switched off the transistor during the transfer of axial energy to the cyclotron mode it had no effect on the observed temperature.

3 Measurements

3.1 Measurement of eigenfrequencies

The unperturbed cyclotron frequency ω_c as required for determining ω_L/ω_c is taken from equation (9) [24,25]

$$\omega_c^2 = \omega_+^2 + \omega_z^2 + \omega_-^2. \tag{21}$$

This equation is accurate even in the presence of electric-field imperfections. All three motional eigenfrequencies of the ion have to be measured precisely. Because of the hierarchy of frequencies

$$\omega_+ > \omega_z > \omega_-, \tag{22}$$

the required precision, however, differs. Aiming to a fractional uncertainty of 10^{-9} in the unperturbed cyclotron frequency, the perturbed cyclotron frequency at 24 MHz has to be determined to 10^{-9} corresponding to an absolute accuracy of 24 mHz. For the 930 kHz axial frequency an accuracy of 7×10^{-7} (0.62 Hz) is necessary while for the 18 kHz magnetron frequency 2×10^{-3} (32 Hz) is sufficient. Since the requirement for the magnetron frequency is rather low, it is determined only once per month whereas the cyclotron and the axial frequencies are measured in each spin-resonance detection cycle.

3.1.1 Perturbed cyclotron frequency

As described in Section 2.5, the perturbed cyclotron frequency ω_+ is measured directly by performing a Fourier transform of the current induced between the two segments of the split correction electrode of the precision trap. A high-resolution Fourier transform, as in Figure 12, shows that the full linewidth is on the order of 25 mHz in a total frequency of 24 MHz, corresponding to a fractional width of 10^{-9}. The line can be fitted to a Lorentzian lineshape and the statistical uncertainty of the center is less than 10^{-10}. The width of the resonance is in agreement with expectations from the residual magnetic field inhomogeneity in the precision trap (see Fig. 13 and Sect. 4).

3.1.2 Axial frequency

The axial frequency is measured while the ion is in thermal equilibrium with the corresponding resonant circuit. The ion signal is observed as a minimum ("dip") in the Fourier transform of the Johnson (thermal) noise of the circuit (Fig. 14). This can be understood by solving the ion's equation of motion under the influence of the fluctuating noise voltage at the trap electrodes as performed by Wineland *et al.* [26]. Here, we give a short intuitive argument. Consider the ion as a driven harmonic oscillator. Any voltage at the trap electrode having the same frequency as the ion oscillation will drive the ion

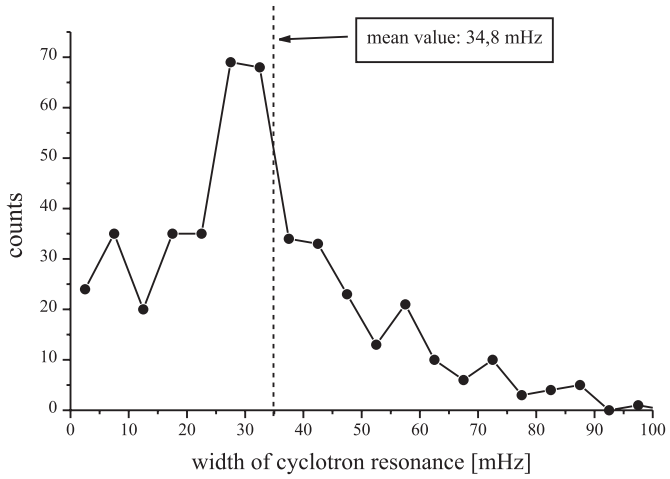

Fig. 13. Histogram of the width of the cyclotron resonances in the precision trap, determined from Lorentzian fits. The average width of 34.8 mHz is consistent with the expected one of 35 mHz derived from the measured magnetic inhomogeneity and the axial temperature in the precision trap. Large widths are exponentially less probable, because they correspond to high axial kinetic energies of the ion.

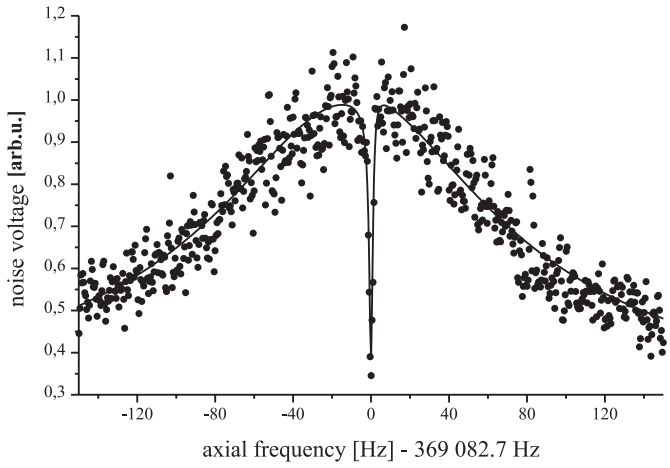

Fig. 14. Axial frequency of a single ion in the analysis trap. It shows up as a minimum in the Fourier transformed noise voltage across the axial tank circuit. The full width of the resonance is 2 Hz. The data acquisition time was 60 s.

strongly. This results in a high a.c. current with opposite phase, shortening the external voltage at this frequency. Consequently the total Johnson noise amplitude at the ion oscillation frequency is reduced. The ion's kinetic energy is not increased through this process compared to the thermal energy of the environment but concentrated in a narrow band. The width of the observed noise minimum is given by the coupling strength γ (Eq. (17)). It has a value of $1/230$ ms^{-1} in our precision trap ($Q = 1\,000$ at $\omega_z = 2\pi \times 930$ kHz) and $1/80$ ms^{-1} in the analysis trap ($Q = 2\,500$ at $\omega_z = 2\pi \times 360$ kHz). The single-ion dip (Fig. 14) has a full width at half maximum of of 2 Hz and 0.7 Hz in the analysis and precision trap, respectively. Its center can be determined to about 5% of the width after

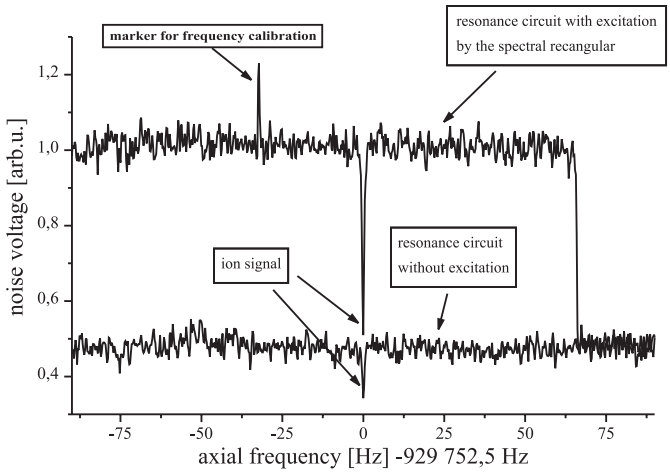

Fig. 15. Increase in the signal-to-noise ratio by exciting the ion motion. The depth of the dip (signal) scales almost linearly with the total voltage across the detection circuit (excitation and Johnson noise), where as the noise depends on the Johnson amplitude only.

averaging for 120 s, which is sufficiently accurate. As will be shown below, a measurement of the axial frequency to a few 100 mHz in the analysis trap is also required in order to detect spin-flip transitions. The determination of the axial frequency in the manner described above takes about 4 minutes during which all parameters have to be kept constant. We reduced this time to less than 60 s by exciting the resonant circuit with a voltage rectangular in frequency space (*i.e.*, in a frequency interval of 100 Hz around the center all frequencies of the voltage have the same amplitude). Figure 15 shows that the noise at the circuit stays constant while the total voltage increases. The signal from the ion is increased by a factor 4 in this example.

3.1.3 Magnetron frequency

The magnetron frequency can not be measured directly. It can be determined, however, by sideband coupling to the axial motion. If we excite the ion by a r.f-drive on one segment of the correction electrode at the difference between the axial and the magnetron frequency ($\omega_z - \omega_-$), the axial motion is heated. This shows up as an easily detectable peak in the Fourier spectrum (Fig. 16).

3.1.4 Optimization of the trap

The eigenfrequencies of the ion in a trap will be shifted if the trapping potential is not perfectly harmonic but contains higher order components (see Sect. 4). In our cylindrical trap, we approximate a quadrupole-type electrical field by tuning the ratio of the voltages at the correction electrodes and the ring electrode. We use two different methods to find the optimum value for this ratio: in the first method we excite the axial oscillation by applying

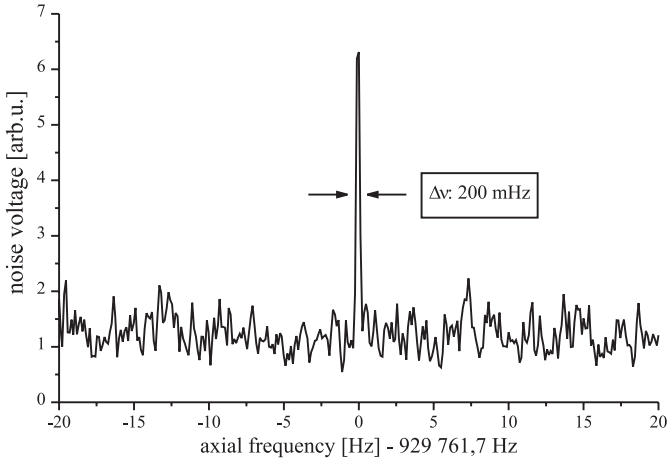

Fig. 16. Measurement of the magnetron frequency. Displayed is the Johnson noise of the axial resonant circuit at the ion's axial frequency. Excitation at the sideband $\omega_z - \omega_-$ leads to a heating of the axial motion and a corresponding increase in the noise voltage.

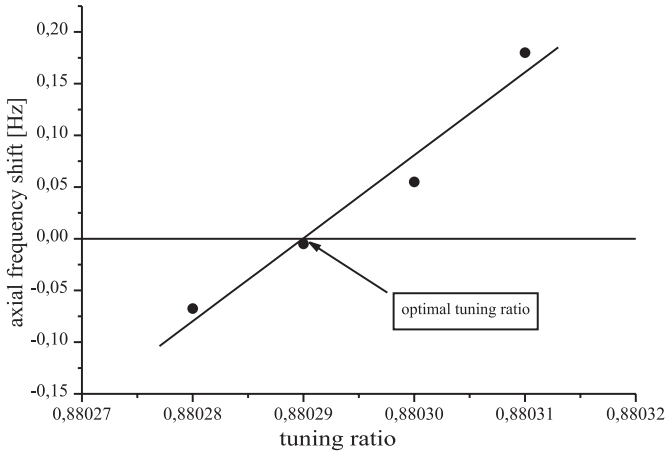

Fig. 17. Determination of the optimum tuning ratio from axial frequency shifts, when the ion's axial temperature is excited from 150 K to 1 500 K. The residual octupole part at a tuning ratio of 0.88029 of the trapping potential has a strength of $C_4 < 10^{-5}$.

a voltage rectangular in frequency space. If the trapping potential is anharmonic, the axial frequency is shifted either to lower or to higher values depending on the sign of the higher-order components in the potential. These components can be changed by applying different voltages to the correction electrodes. Defining a tuning ratio as the ratio between the correction voltage an the trapping voltage, we find the optimal tuning ratio when the axial frequency is not shifted after excitation (Fig. 17). Another possibility to monitor the quality of the trapping potential is to measure the depth of the dip in the power spectrum of the axial tank circuit from a stored single ion. It has its highest value when the trap is harmonic. Both methods give the same optimum tuning ratio within their error margins. We arrive at a value for the octupole term C_4 of less than 10^{-5}. Due to the special electrode

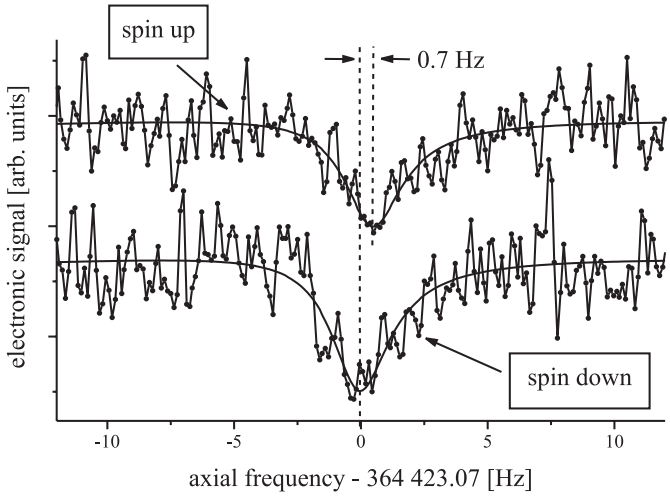

Fig. 18. Axial frequency measurements for spin up and spin down. The axial frequency differs for the two spin direction by about 0.7 Hz.

geometry [21], the dodecapole term C_6 amounts then also to only 10^{-3}. These small higher-order contributions shift the cyclotron frequency as calculated from equation (21) by less than 10^{-10}. Other higher order terms in the potential need not to be considered.

3.2 Spin flip transitions

Transitions of the spin direction of the bound electron can be induced by a microwave field. At our magnetic field of 3.8 T the resonance frequency (Larmor precession frequency) is about 104 GHz. It is determined by recording the spin-flip rate of the electron versus the frequency of the exciting field. The spin-flip transitions are observed using the technique developed in the electron $g-2$ experiment by Dehmelt *et al.* [29] and first demonstrated for atomic ions in [19]. A quadratic inhomogeneity in the magnetic field (*magnetic bottle*) produced by a ferromagnetic ring electrode in the analysis trap (see Fig. 2) leads to a quadratic dependence of the magnetic energy E_{mag} on the z-coordinate (*cf.* Eq. (12))

$$E_{\mathrm{mag}} = -\boldsymbol{\mu} \cdot \mathbf{B} = -\mu_z(B_0 + B_2 z^2 + \cdots). \qquad (23)$$

The ion's axial oscillation frequency is given by the sum of the electric potential and the magnetic potential. Both potentials depend on the square of the coordinates and thus the total potential is harmonic. Because of the different sign of the magnetic potential for the two spin directions, the axial frequency is slightly different for spin up and spin down (*continuous Stern-Gerlach effect*) [30]. The resulting difference of the axial frequency of $^{12}C^{5+}$ at our measured value of the quadratic magnetic field component ($B_2 = 10$ mT/mm^2) is calculated to amount to about 0.7 Hz at a total axial frequency of 360 kHz which is experimentally verified (Fig. 18). If we vary the microwave-field frequency around the expected Larmor frequency in the analysis trap and record the number of

spin flips per unit time we obtain a resonance curve. The lineshape, however, is broadened and made asymmetric by the inhomogeneity of the magnetic field at this position. Using a proper line shape formula the resonance frequency was determined to a precision of about 10^{-6} [19].

A significant improvement has been obtained by introducing a *double-trap technique*. We transfer the ion to the precision trap where the spin-flip transitions are induced in the homogeneous part of the magnetic field. Then we transfer it back to the analysis trap to determine the spin direction. This reduces the width of the resonance by 3 orders of magnitude.

3.2.1 Transfer of the ion

The transfer between the two traps is achieved by changing the voltages at the different electrodes continuously in such a way that a potential minimum is maintained. The variation of the minimum position in time is slow compared to the period of the axial frequency. It takes about 1 s. A single ion and ion clouds could be transferred more than 10 000 times between the precision and analysis trap without any ion loss. For a single ion we observed no increase of the magnetron radius after 1 000 transfers, whereas for ion clouds some magnetron heating takes place. This is due to ion-ion interaction during the transport.

3.2.2 Measurement cycle

For the measurement of the frequency ratio ω_L/ω_c we use the following procedure (see Fig. 19): after the preparation of a single ion, all motional modes are cooled to the minimum obtainable temperatures. Then we optimize the trapping potential of both traps as explained in Section 3.1.4. This is necessary because after each creation of ions the surface charges on the electrodes may change slightly.

We then start the measurement cycle: at first the ion's spin direction is determined in the analysis trap by inducing spin flips and observing the corresponding change of 0.7 Hz in the axial frequency. Then the ion is transferred to the precision trap. Here, again spin flips are induced by a microwave field. Simultaneously, the cyclotron frequency is recorded. Finally the ion is transferred back to the analysis trap where we determine the spin direction again. The directions of the spin before and after the transfer reveals whether a spin flip took place in the precision trap (see Fig. 20). A single measurement of the axial frequency in the analysis trap, however, is not sufficient to determine the spin direction without any doubt because the axial frequency might have changed not only by a spin flip but also by instabilities in the applied voltage or a change in cyclotron energy. Inducing a sequence of two spin flips reduces any ambiguity substantially.

Parallel to the attempt to induce a spin-flip transition we measure simultaneously the cyclotron frequency

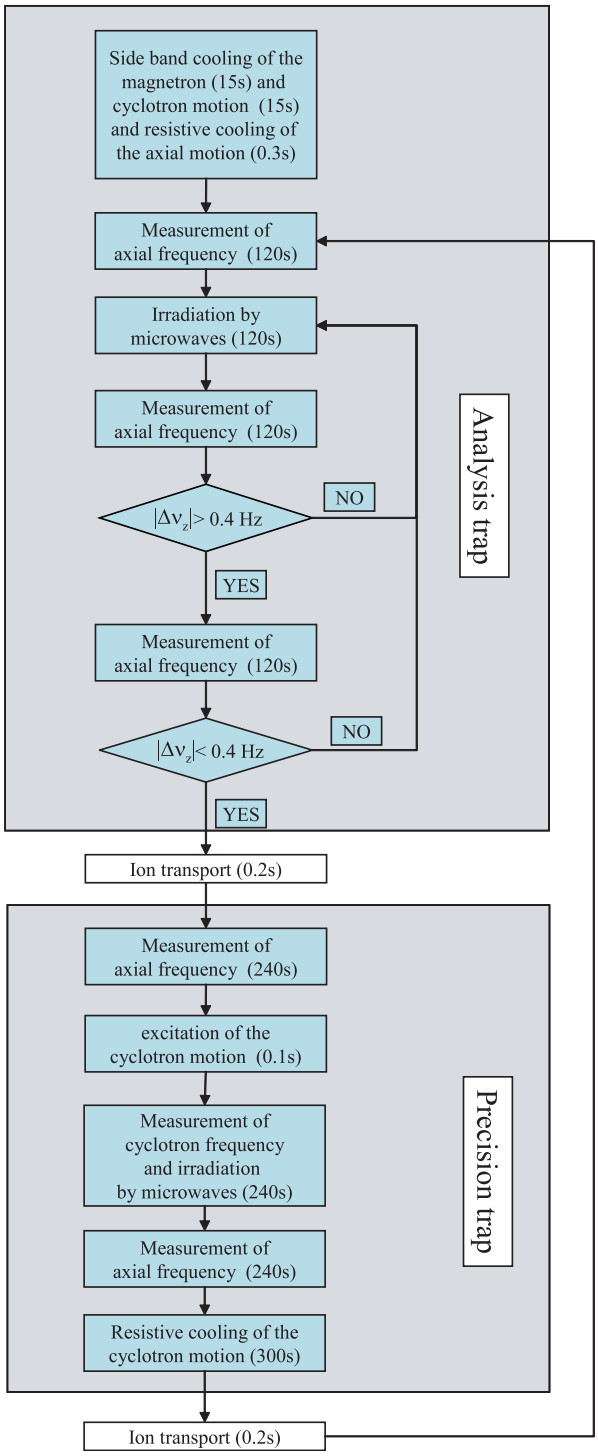

Fig. 19. Measurement cycle.

of the ion (Eq. (4)). As a first step we excite the perturbed cyclotron motion to an energy of 5–20 eV (typical parameters of the ion motion are compiled in Tab. 2). This induces a current large enough to be measured. We then let the ion's cyclotron motion cool down resistively to energies E_+ between 1–5 eV, at which we take the data. The cooling process is monitored by the strength of the induced current and we stop it at the desired energy by

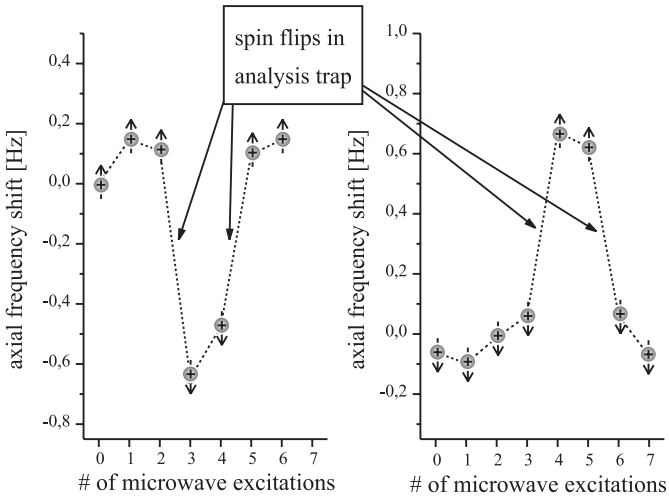

Fig. 20. Determination of the spin direction. In the analysis trap, the direction of the spin is determined by irradiating the ion with microwaves and measuring the axial frequency subsequently. A frequency change of 0.7 Hz downwards indicates a spin transition from up to down, and *vice versa*.

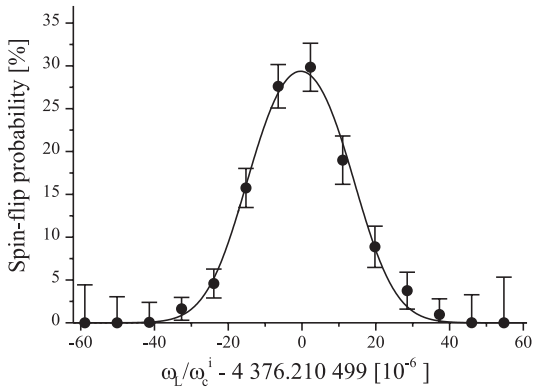

Fig. 21. $\omega_{\rm L}/\omega_{\rm c}$ resonance measured in the precision trap. Plotted is the spin-flip probability *versus* the ratio of the microwave and the cyclotron frequency $\omega_{\rm L}/\omega_{\rm c}$, corrected for the cyclotron energy E_+ according to equation (45) by $-2.4 \times 10^{-6} E_+/\mathrm{eV}$ (*cf.* Fig. 29). The measurement includes 1 000 attempts to induce spin flips. The total measurement time was one month. The solid line is a fit to a Gaussian. The dashed line is a fit to a convolution of a Gaussian and a Boltzmann distribution (Eq. (34)). Both models take saturation effects into account. The error margins are deduced by assuming a binomial distribution of the spin-flip probability.

Table 2. Typical amplitude r, frequency ω and energy E of the ion motion during the measurements.

	r [μm]	ω [kHz]	E [meV]
Cyclotron	46	$2\pi\times$ 24 075	3 000
Axial	50	$2\pi\times$ 929	5
Magnetron	93	$2\pi\times$ 18	–10

switching off the cooling circuit. We then measure the axial frequency (Sect. 3.1.2). This is necessary because we have to calculate the unperturbed cyclotron frequency $\omega_{\rm c}$ from equation (21). During the measurements of the axial frequency, the cyclotron resonant circuit is detuned by changing its capacitance by GaAs-switches, so that the cyclotron energy stays constant leaving the axial frequency stable as well. We vary $\omega_{\rm mw}/\omega_{\rm c}$ by changing the 104 GHz microwave frequency $\omega_{\rm mw}$ around the expected value for $\omega_{\rm L}$. While the ion is irradiated by microwaves, we simultaneously measure the perturbed cyclotron frequency. This takes 80 s, corresponding to a Fourier limit of 12 mHz. We then repeat the measurement of the axial frequency and cool the ion's cyclotron motion by coupling it to the axial motion employing an r.f.-field at $\omega_+ - \omega_z$ (similar to the sideband-coupling technique described in Sect. 2.8.1). Then the axial frequency is measured a third time. The shift $\Delta\omega_z$ of the axial frequency between the average of the first two measurements and the third one is a measure for the cyclotron energy at which the ion has been irradiated by microwaves (*cf.* Eqs. (14, 38)). This knowledge is required to account for a small shift of the value of $\omega_{\rm L}/\omega_{\rm c}$ depending on the cyclotron energy. It mainly arises from a residual inhomogeneity of the magnetic field in the precision trap.

Finally, the ion is transferred back to the analysis trap where the direction of the spin is determined again in the same way as described above. Comparing the spin direction before and after the transfer to the precision trap allows now to decide whether in the precision trap a spin-flip has taken place or not (Fig. 20). More precisely we distinguish between an odd and even number (including 0) of spin-flips. In case of too high amplitude of the inducing microwave field the spins are in arbitrary direction after transfer to the analysis trap. We keep the amplitude to such a value that the maximum spin-flip probability is around 30% to avoid saturation by multiple spin-flips. From the sideband cooling of the cyclotron energy in the precision trap, we get a thermal distribution of the cyclotron energy with a mean value of 5 meV (see Sect. 2.9 and Fig. 11). In the analysis trap this leads to a spread of the axial frequency of about 200 Hz (see Fig. 11). This overshadows by far the effect of a spin flip and makes it necessary to change the storage potential each time so that the ion's axial frequency matches the resonance of the circuit. The measurement cycle is fully automated and takes 20–30 minutes for one single event.

The resonance obtained when plotting the spin-flip probability *versus* the applied frequency is much more symmetric than resonances obtained in analysis trap alone. The fractional width of these resonances is 2×10^{-8} and their center can be determined to a precision of better than 10^{-9} (see Fig. 21).

4 Systematic uncertainties

Apart from statistical uncertainties, the final accuracy is determined by the extent to which possible systematical errors can be accounted for. Table 3 lists the effects which we have considered and which we are going to discuss in the following sections. The largest contribution comes

Table 3. Systematic uncertainties of ω_L/ω_c which are considered. The corresponding sections are indicated in parentheses. All uncertainties are given in relative units.

asymmetry of resonance (4.1.2)	2×10^{-10}
measurement of cyclotron energy (4.2)	2×10^{-10}
electric field imperfections (4.4)	1×10^{-10}
cavity-QED shifts (4.5)	$\approx 10^{-13}$
interaction with image charges (4.5)	3×10^{-11}
relativistic corrections (4.6)	1×10^{-12}
magnetron energy (4.7)	1×10^{-11}
shift by standing microwave field (4.7)	$< 10^{-14}$
stability of quartz oscillators (4.7)	1×10^{-10}
grounding of apparatus (4.7)	4×10^{-11}
saturation of spin-flip transition	5×10^{-12}
spectral purity of microwaves	5×10^{-13}
damping of ion motion	$\approx 10^{-20}$
total (quadrature sum)	3×10^{-10}

Table 4. Corrections which are included in the final evaluation of the experimental value for ω_L/ω_c.

experimental value	4376.210 500 2
interaction with image charges (4.5)	−0.000 001 2
shift due to grounding (4.7)	−0.000 000 3
cyclotron energy measurement (4.2)	+0.000 000 3
final experimental value	4376.210 499 0

from our understanding of the resonance line shape which is affected by a small residual inhomogeneity of the magnetic field in the precision trap. We are also going to discuss some corrections that we have to apply to our final experimental value (see Tab. 4).

4.1 Lineshape

4.1.1 Basic lineshapes

In a perfectly homogeneous magnetic field, the cyclotron and Larmor resonances would be described by a Lorentzian lineshape. The slight inhomogeneity of the field in the precision trap caused by the residual influence of the nickel ring in the analysis trap, 27 mm apart, leads to distortions. The shape of both resonances in an inhomogeneous magnetic field of the form given by equation (12) was calculated by Brown [31,32].

In our experiment for each test of a certain ratio of ω_{mw}/ω_c, the influence of the cyclotron energy can be neglected because the ion is decoupled from the environment during the measurement. The axial mode, however, is strongly coupled to the resonant circuit with a time constant of $1/\gamma = 233$ ms. The basic broadening process is the dependence of the average field on the thermally fluctuating axial energy (Eqs. (15, 16)). For this reason, the axial energy distribution should show up in the lineshape.

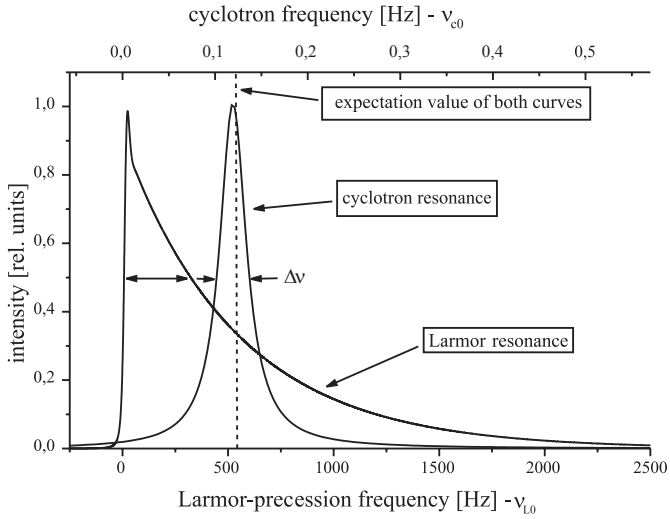

Fig. 22. Theoretical lineshape of the Larmor and the cyclotron resonances calculated from equation (26). The shape of the Larmor resonance reflects the energy distribution of the axial mode.

This becomes significant only when the frequency fluctuations ($\Delta\omega_L$ or $\Delta\omega_+$) due to the axial energy fluctuations are much larger than the time constant γ (Eq. (17)) for axial energy change. For our experiment with $\langle E_z \rangle = 70$ K and a magnetic field of 4 T, this condition holds only for the Larmor frequency at 104 GHz ($\Delta\omega_L \approx 80\gamma$). In this case the resonance shape $\chi(\omega'_L)$ is given by a Boltzmannian exponential

$$\chi(\omega'_L) = \frac{\theta(\omega'_L - \omega_{L0})}{\Delta\omega} \exp\left(-\frac{\omega'_L - \omega_{L0}}{\Delta\omega_L}\right). \qquad (24)$$

Here ω_{L0} denotes the Larmor frequency for vanishing axial energy. The calculated half width of the resonance for our set of parameters is $\Delta\omega_L/\omega_{L0} = 3 \times 10^{-9}$.

For the cyclotron motion at 24 MHz we have at $\langle E_z \rangle = 70$ K, $\Delta\omega_+ \approx 1/5\,\gamma$, and the frequency fluctuations $\Delta\omega_+$ are smaller than the energy-exchange time constant. In this case, the lineshape can be approximated by a Lorentzian which arises from *motional averaging* [33–35]

$$\chi(\omega'_+) = \frac{\Delta\omega_+{}'^2/\pi\gamma}{(\omega'_+ - \omega_{+0} - \Delta\omega_+)^2 + (\Delta\omega_+{}'^2/\gamma)^2}. \qquad (25)$$

The full half width of this resonance line (Fig. 22) is $\Delta\omega_c/\omega_{c0} = 1.5 \times 10^{-9}$. The fact that the cyclotron resonance is narrower than the Larmor resonance is understandable since for a low frequency it takes longer until the frequency is defined with the same relative accuracy as for a higher one. In our case the ion does not spend sufficient time at high axial energies (corresponding to high cyclotron frequencies) to contribute to the wings of the spectral line. In Figure 22 we display the two basic lineshapes for our experimental parameters.

In the intermediate region, $\Delta\omega_+ \approx \gamma$, which is the case for axial temperatures of about 360 K, one has to

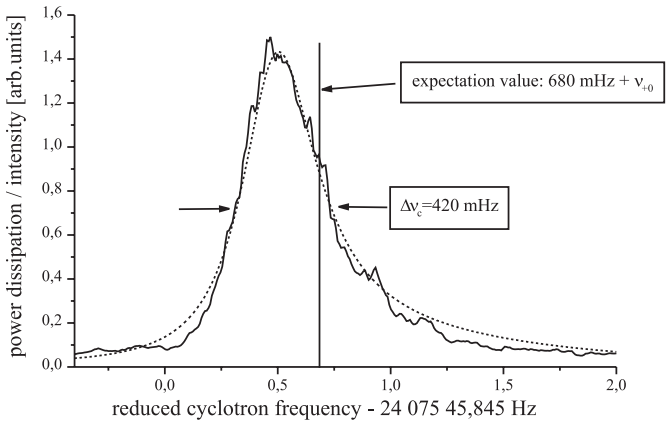

Fig. 23. Cyclotron resonance for an axial temperature of 350 K. The fit function (dashed line), using amplitude, resonant frequency and background as free parameters, is given by equation (26).

use a power series as developed by Brown to describe the lineshape [31,32]:

$$\chi(\omega) = \frac{4}{\pi}\mathrm{Re}\frac{\gamma'\gamma}{(\gamma'+\gamma)^2}\sum_{n=0}^{\infty}\frac{(\gamma'-\gamma)^{2n}(\gamma'-\gamma)^{-2n}}{(n+\frac{1}{2})\gamma' - \frac{1}{2}\gamma - \mathrm{i}(\omega-\omega_0)}\cdot \tag{26}$$

The assumptions made by Brown were a Boltzmannian distribution of the axial energy with the coupling constant γ to the thermal bath and a magnetic field perturbation described by equation (12). γ' is defined by

$$\gamma' = \sqrt{\gamma^2 + 4\mathrm{i}\gamma\Delta\omega}. \tag{27}$$

$\Delta\omega$ can be interpreted as the line shift which occurs when the ion has an axial energy equal to that of the energy's expectation value.

Equations (24, 25) are obtained in the limits $\Delta\omega \gg \gamma$ and $\Delta\omega \ll \gamma$, respectively. Figure 23 indicates that Brown's model gives a correct description of the lineshape at $\gamma \approx \Delta\omega$. In the fit we have assumed an ion temperature of 350 K, which was derived from a separate measurement (see Sect. 2.9).

4.1.2 Lineshape of the $\omega_\mathrm{L}/\omega_\mathrm{c}$ resonance

We obtain an "$\omega_\mathrm{L}/\omega_\mathrm{c}$ resonance" by plotting the spin-flip probability *versus* the ratio $\omega_\mathrm{mw}/\omega_\mathrm{c}$. The theoretical lineshape for this resonance can be derived using the results from the Larmor- and cyclotron resonances. The distribution of the Larmor frequencies is obtained from equation (24)

$$P_\mathrm{L}\left(\frac{\delta\omega_\mathrm{L}}{\omega_\mathrm{L0}}\right) = \frac{\theta(\delta\omega_\mathrm{L})}{\Delta\omega_\mathrm{L}}\exp\left(-\frac{\delta\omega_\mathrm{L}}{\Delta\omega_\mathrm{L}}\right)\cdot \tag{28}$$

For each spin-state measurement, we obtain a complete cyclotron resonance and determine the average cyclotron frequency. For the distribution of the cyclotron frequencies we assume a Gaussian,

$$P_\mathrm{c}\left(\frac{\delta\omega_\mathrm{c}}{\omega_\mathrm{c}}\right) = \frac{1}{\sqrt{\pi}\Delta\omega_\mathrm{c}}\exp\left(-\frac{\delta\omega_\mathrm{c}^2}{\Delta\omega_\mathrm{c}^2}\right), \tag{29}$$

where $\Delta\omega_\mathrm{c}$ is the variance of the cyclotron frequency measurements.

We have not yet taken into account that the cyclotron frequency ω_c is a measure of the average magnetic field whereas the Larmor frequency ω_L0 corresponds to the magnetic field for vanishing axial energy (Fig. 22). The shift of the average magnetic field is connected to the width of the Larmor resonance $\Delta\omega_\mathrm{L}$,

$$\frac{\overline{\Delta B}}{B_0} = \frac{\Delta\omega_\mathrm{L}}{\omega_\mathrm{L0}}\cdot \tag{30}$$

Taking this into account we get

$$P_\mathrm{c}\left(\frac{\delta\omega_\mathrm{c}}{\omega_\mathrm{c}}\right) = \frac{1}{\sqrt{\pi}\Delta\omega_\mathrm{c}}\exp\left(-\frac{(\delta\omega_\mathrm{c} - \frac{\Delta\omega_\mathrm{L}}{\omega_\mathrm{L0}}\omega_\mathrm{c})^2}{\Delta\omega_\mathrm{c}^2}\right)\cdot \tag{31}$$

Shifts $\delta\omega_\mathrm{L} = \omega'_\mathrm{L} - \omega_\mathrm{L0}$ of the Larmor frequency and of the cyclotron frequency ($\delta\omega_\mathrm{c} = \omega'_\mathrm{c} - (\omega_\mathrm{c0} + \Delta\omega_\mathrm{c})$) enter in the following way into the determination of $\omega_\mathrm{L}/\omega_\mathrm{c}$:

$$\frac{\delta(\omega_\mathrm{L}/\omega_\mathrm{c})}{\omega_\mathrm{L}/\omega_\mathrm{c}} == \frac{1}{(\omega_\mathrm{L}/\omega_\mathrm{c})}\left(\frac{\delta\omega_\mathrm{L}}{\omega_\mathrm{L}} - \frac{\delta\omega_\mathrm{c}}{\omega_\mathrm{c}}\right)\cdot \tag{32}$$

Inserting the distributions for ω_L and ω_c into equation (32) gives the probability to obtain a spin flip at the difference $\delta(\omega_\mathrm{L}/\omega_\mathrm{c})$ from the "true" value of $\omega_\mathrm{L}/\omega_\mathrm{c}$,

$$\begin{aligned}
&P\left(\frac{\delta(\omega_\mathrm{L}/\omega_\mathrm{c})}{\omega_\mathrm{L}/\omega_\mathrm{c}}\right) = P\left(\frac{\delta\omega_\mathrm{L}}{\omega_\mathrm{L0}} - \frac{\delta\omega_\mathrm{c}}{\omega_\mathrm{c}}\right)\\
&= \int_{-\infty}^{\infty}\int_{-\infty}^{\infty}\mathrm{d}\frac{\delta\omega_\mathrm{L}}{\omega_\mathrm{L0}}\mathrm{d}\frac{\delta\omega_\mathrm{c}}{\omega_\mathrm{c}}\,P_\mathrm{L}\left(\frac{\delta\omega_\mathrm{L}}{\omega_\mathrm{L0}}\right)P_\mathrm{c}\left(\frac{\delta\omega_\mathrm{c}}{\omega_\mathrm{c}}\right)\Big|_{\frac{\delta\omega_\mathrm{L}}{\omega_\mathrm{L0}} - \frac{\delta\omega_\mathrm{c}}{\omega_\mathrm{c}} = \frac{\delta(\omega_\mathrm{L}/\omega_\mathrm{c})}{\omega_\mathrm{L}/\omega_\mathrm{c}}}\\
&= \int_{-\infty}^{\infty}\mathrm{d}\frac{\delta\omega_\mathrm{L}}{\omega_\mathrm{L0}}\,P_\mathrm{L}\left(\frac{\delta\omega_\mathrm{L}}{\omega_\mathrm{L0}}\right)P_\mathrm{c}\left(\frac{\delta\omega_\mathrm{L}}{\omega_\mathrm{L0}} - \frac{\delta(\omega_\mathrm{L}/\omega_\mathrm{c})}{\omega_\mathrm{L}/\omega_\mathrm{c}}\right)\\
&= \frac{\theta(\delta\omega_\mathrm{L})}{\sqrt{\pi}\Delta\omega_\mathrm{L}\Delta\omega_\mathrm{c}}\int_{-\infty}^{\infty}\mathrm{d}\frac{\delta\omega_\mathrm{L}}{\omega_\mathrm{L0}}\left(-\frac{\delta\omega_\mathrm{L}}{\Delta\omega_\mathrm{L0}}\right)\\
&\quad\times\exp\left(-\frac{\omega_\mathrm{c}^2}{\Delta\omega_\mathrm{c}^2}\left(\frac{\delta\omega_\mathrm{L}}{\omega_\mathrm{L0}} - \frac{\delta(\omega_\mathrm{L}/\omega_\mathrm{c})}{\omega_\mathrm{L}/\omega_\mathrm{c}} - \frac{\Delta\omega_\mathrm{L}}{\omega_\mathrm{L0}}\right)^2\right)\cdot
\end{aligned} \tag{33}$$

After integration we get

$$\begin{aligned}
&P\left(\frac{\delta(\omega_\mathrm{L}/\omega_\mathrm{c})}{\omega_\mathrm{L}/\omega_\mathrm{c}}\right) =\\
&\quad\frac{\omega_\mathrm{L0}}{2\delta\omega_\mathrm{L}}\exp\left(-1 + \frac{\delta\omega_\mathrm{c}^2}{\omega_\mathrm{c}^2}\frac{4\omega_\mathrm{L0}^2}{\delta\omega_\mathrm{c}^2} - \frac{\omega_\mathrm{L0}^2}{\delta\omega_\mathrm{L}^2}\frac{\delta(\omega_\mathrm{L}/\omega_\mathrm{c})}{\omega_\mathrm{L}/\omega_\mathrm{c}}\right)\\
&\quad\times\left[\mathrm{erf}\left(\frac{\delta\omega_\mathrm{L}}{\omega_\mathrm{L0}}\frac{\omega_\mathrm{c}}{\delta\omega_\mathrm{c}} - \frac{\delta\omega_\mathrm{c}}{\omega_\mathrm{c}}\frac{\omega_\mathrm{L0}}{2\delta\omega_\mathrm{L}} + \frac{\omega_\mathrm{c}^2}{\delta\omega_\mathrm{c}^2}\frac{\delta(\omega_\mathrm{L}/\omega_\mathrm{c})}{\omega_\mathrm{L}/\omega_\mathrm{c}}\right) - 1\right].
\end{aligned} \tag{34}$$

Here, $\mathrm{erf}(x)$ denotes the error function, defined as

$$\mathrm{erf}(x) \equiv \frac{2}{\sqrt{\pi}} \int_0^x \mathrm{e}^{-t^2}\,\mathrm{d}t. \tag{35}$$

This lineshape is determined by the magnetic field inhomogeneity through $\delta\omega_\mathrm{L}/\omega_\mathrm{L0}$ and by the uncertainty of the cyclotron frequency measurements $\delta\omega_\mathrm{c}/\omega_\mathrm{c}$. The asymmetry of the lineshape is given by the ratio $\delta\omega_\mathrm{L}/\delta\omega_\mathrm{c}$. One important observation is that the expectation value of equation (34) is always zero. This means that an $\omega_\mathrm{L}/\omega_\mathrm{c}$ extracted by any symmetrical fit function will not deviate much from the correct value.

We have not taken into account any effect of saturation on the theoretical lineshape. It arises from the fact that we can only distinguish between an even or an uneven number of spin flips. The actually observed rate $R_\mathrm{O}(t)$ is related to the true rate R by [24]

$$R_\mathrm{O}(t) = \frac{1}{2}\left(1 - \mathrm{e}^{-2Rt}\right). \tag{36}$$

Obviously the maximal observable spin-flip probability for the non-coherently driven transition is 50%.

Figure 21 shows a least-squares fitted resonance shape according to equation (34), taking into account the saturation effects according to equation (36), to the experimentally obtained data of an $(\omega_\mathrm{L}/\omega_\mathrm{c})$ resonance. The $(\omega_\mathrm{L}/\omega_\mathrm{c})$ resonance was obtained by correcting each event (spin flip or no spin flip) for the corresponding cyclotron energy according to Section 4.2. For the parameter $\delta\omega_\mathrm{c}/\omega_\mathrm{c}$ describing the uncertainty in the cyclotron frequency, we obtain $\delta\omega_\mathrm{c}/\omega_\mathrm{c} = 3.13\,(13) \times 10^{-9}$, for $\delta\omega_\mathrm{L}/\omega_\mathrm{L}$ characterizing the magnetic inhomogeneity (B_2) we obtain $\delta\omega_\mathrm{L}/\omega_\mathrm{L} = 1.64\,(18) \times 10^{-9}$. This value is a factor of 3 smaller than expected from the measured value $B_2 = 8$ mT/mm^2 (see Sect. 4.1.3). In Figure 21 we also show a fit using a completely symmetric function (a Gaussian with saturation effects) for comparison. The extracted $(\omega_\mathrm{L}/\omega_\mathrm{c})$ differs by less than 1×10^{-10} (all uncertainties given for $(\omega_\mathrm{L}/\omega_\mathrm{c})$ are in relative units), indicating that the extracted $(\omega_\mathrm{L}/\omega_\mathrm{c})$ values are not very sensitive to the model. This is expected since the expectation value of the $(\omega_\mathrm{L}/\omega_\mathrm{c})$ resonance does not depend on the magnetic inhomogeneity.

To investigate the theoretical model further, we increased the axial ion energy by applying white noise to the resonant circuit during the irradiation by microwaves up to a factor 6 to $T_\mathrm{ax} = 340$ K. The obtained $(\omega_\mathrm{L}/\omega_\mathrm{c})$ resonance is shown in Figure 24. At these high axial energies the lineshape is broadened and it is easier to determine the applicability of a fitting function. A simple Gaussian (solid line) does not fit the data well, in contrast to the fit function given by equation (34) (dashed line). However, both extracted values for $(\omega_\mathrm{L}/\omega_\mathrm{c})$ differ only by 1 part in 10^{-9}. We checked also whether the extracted values for $(\omega_\mathrm{L}/\omega_\mathrm{c})$ depend on the axial energy (Fig. 25). We observed no significant dependence, as expected from the smallness of B_2 in the precision trap.

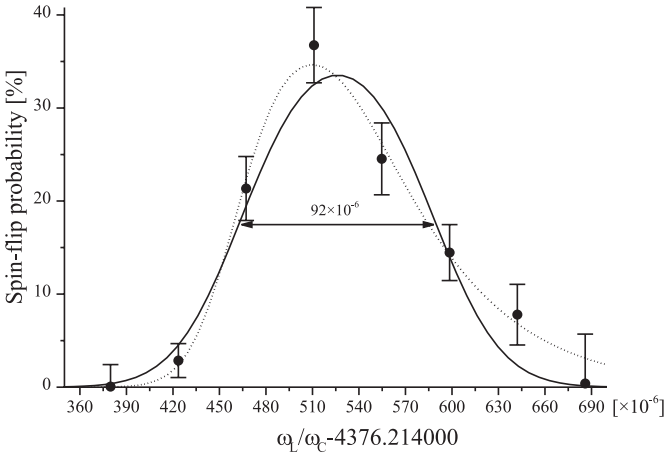

Fig. 24. $(\omega_\mathrm{L}/\omega_\mathrm{c})$ resonance at an axial temperature of 340 K. The solid line is a fit using a Gaussian inserted into equation (36). It yields $\omega_\mathrm{L}/\omega_\mathrm{c} = 4376.210\,500\,2$ (46). The dashed line is a fit according to equations (34) and (36) and yields $\omega_\mathrm{L}/\omega_\mathrm{c} = 4376.210\,508\,3$ (38).

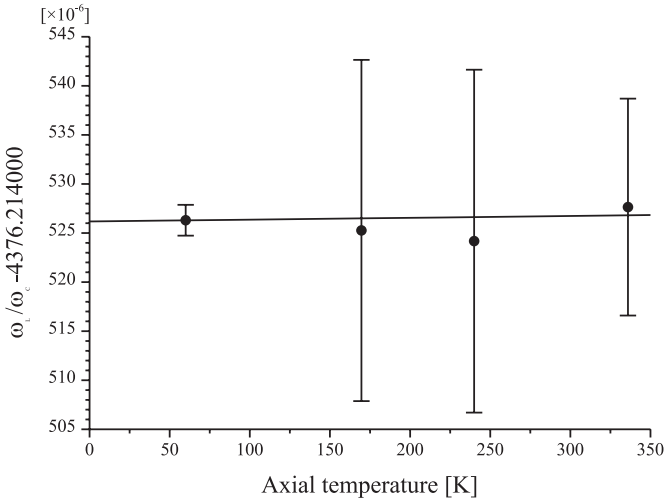

Fig. 25. Extrapolation of $(\omega_\mathrm{L}/\omega_\mathrm{c})$ to zero axial energy. The slope is consistent with zero.

4.1.3 Measurements of the magnetic field inhomogeneity

A determination of the residual inhomogeneity of the magnetic field in the precision trap, mainly caused by the nickel ring electrode in the analysis trap, is crucial for a proper analysis of the systematic error in our experiment. We use three different methods for determining the magnetic field inhomogeneities.

– The cyclotron frequency of the ion is measured at different positions along the z-axis. We shift the ion along the z-axis by applying an additional electric field gradient to the trapping potential. Measuring the cyclotron frequency at different positions yields the spatial magnetic field profile (Fig. 26). We obtain a linear field gradient B_1 of 60.4 (2) μT/mm. For B_2 we get 41.5 (50) μT/mm^2, however with a large error margin

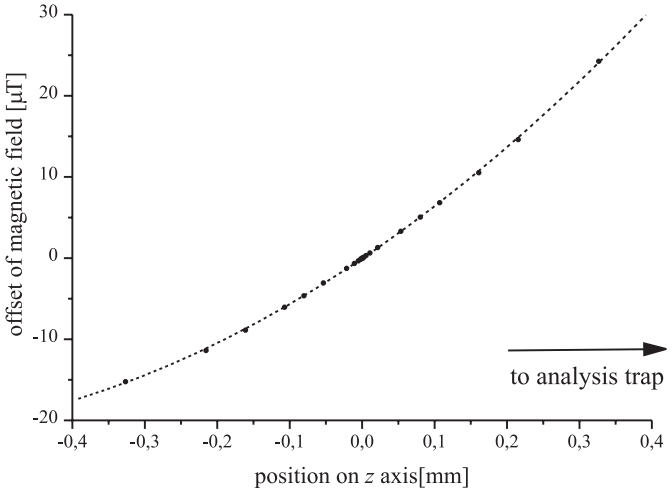

Fig. 26. Spatial magnetic field distribution in the precision trap. From this measurement the linear field gradient B_1 can be extracted. It amounts to 60.4 (2) μT/mm.

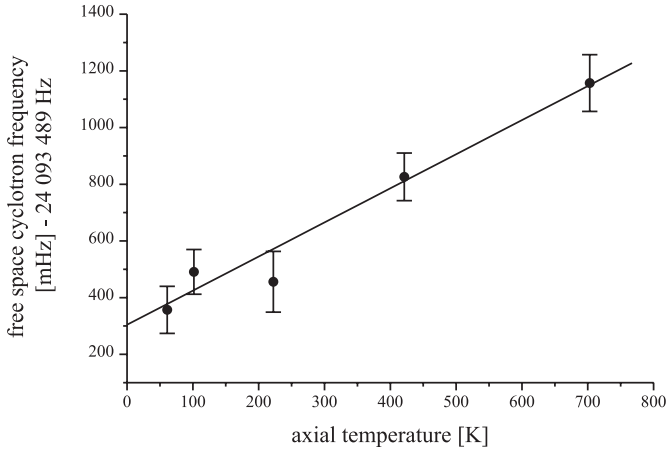

Fig. 27. Free space cyclotron frequency as a function of the axial oscillation amplitude. The measurement was performed by electronically increasing the axial energy by broad band excitation (as explained in Sect. 3.1.2) to a different temperature and extracting from equation (21) the unperturbed cyclotron frequency.

arising mainly from the limited knowledge of the electric field.

– The axial frequency is determined for different cyclotron energies. Equation (14) gives the relation between the cyclotron energy and the axial frequency shift for a given size of B_2. For a given cyclotron energy, we measure the axial frequency shift in the precision and the analysis trap. The ratio of the two frequency shifts equals the ratio of the B_2-terms in the precision and analysis trap. The large B_2-term in the analysis trap is known both from measurement and calculations to be equal to 10 (1) mT/mm^2. We obtain for the precision trap

$$B_2 = 8.2\,(9)\ \mu\mathrm{T/mm}^2. \tag{37}$$

From equation (14) we get the calibration for the cyclotron energy

$$E_+ = 2.18\,(24)\ \mathrm{eV\,s}\,\frac{\Delta\omega_z}{2\pi}\cdot \tag{38}$$

– The cyclotron frequency is measured as a function of the axial oscillation amplitude of the ion (Fig. 27). Using equation (15) we obtain from our measurement $B_2 = 7.0\ (2.2)\ \mu\mathrm{T/mm}^2$, in agreement with equation (37). The uncertainty is dominated by the determination of the axial oscillation amplitude.

4.2 Dependence of $(\omega_\mathrm{L}/\omega_\mathrm{c})$ on the cyclotron energy

For a measurement of the perturbed cyclotron frequency, the energy in the cyclotron mode has to be raised to about 1 eV in order to get a reasonable signal strength. This shifts the eigenfrequencies of the axial and perturbed cyclotron motions (Eqs. (13) and (15))

$$\omega_+ \rightarrow \omega_+ - \frac{\omega_z}{\omega_+}\,\Delta\omega_z, \tag{39}$$

$$\omega_z \rightarrow \omega_z + \Delta\omega_z. \tag{40}$$

Inserting these shifts into equation (21) leads to

$$\begin{aligned}\Delta\omega_\mathrm{c} &= \sqrt{(\omega_+ + \Delta\omega_+)^2 + (\omega_z + \Delta\omega_z)^2 + \omega_-^2} - \omega_\mathrm{c}\\ &\approx \sqrt{\omega_+^2 - 2\omega_z\,\Delta\omega_z + \omega_z^2 + 2\omega_z\,\Delta\omega_z + \omega_-^2} - \omega_\mathrm{c}\\ &= 0.\end{aligned} \tag{41}$$

Thus to first order the cyclotron frequency is independent of the ion's cyclotron energy. In contrast, the Larmor frequency changes with the cyclotron energy because the radius of the cyclotron motion increases with increasing cyclotron energy and thus the average magnetic field will be different for a non-vanishing B_2 term (Eq. 16),

$$\Delta\omega_\mathrm{L} = -\frac{\omega_z}{\omega_+^2}\omega_\mathrm{L}\,\Delta\omega_z. \tag{42}$$

To test these relations, we excited the ion to cyclotron energies between 1 and 50 eV, corresponding to shifts $\Delta\omega_z$ of the axial frequency between $2\pi \times 0.5$ and $2\pi \times 25$ Hz. At this cyclotron energies the perturbed cyclotron and the axial frequency were measured (Fig. 28). From equations (14) and (15) we expect a slope of

$$\frac{\Delta\omega_+}{\omega_+} = -\frac{1}{\omega_+}\frac{\omega_z^2}{\omega_+^2}\,\Delta\omega_z = -1.6\times10^{-9}\ \mathrm{s}\times\frac{\Delta\omega_z}{2\pi}\cdot \tag{43}$$

The measured slope of $\Delta\omega_+/\omega_+ = -2.4\ (1)\times10^{-9}\ \mathrm{s}\times \Delta\omega_z/2\pi$ is larger than our expectation. This discrepancy can be attributed to a non-perfect axial symmetric magnetic field.

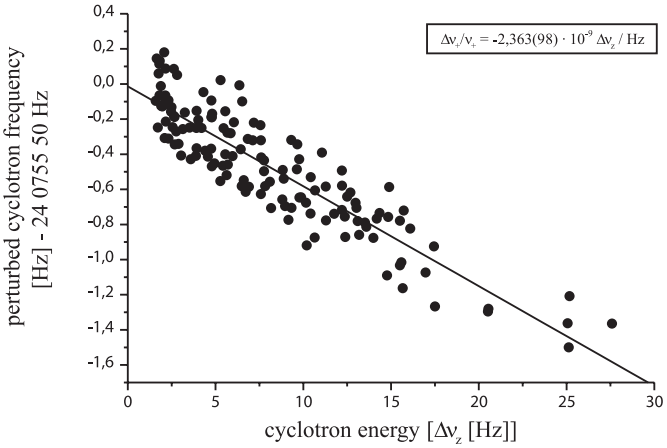

Fig. 28. The reduced cyclotron frequency as a function of the cyclotron energy, measured in units of the axial frequency shift according to equations (15) and (39).

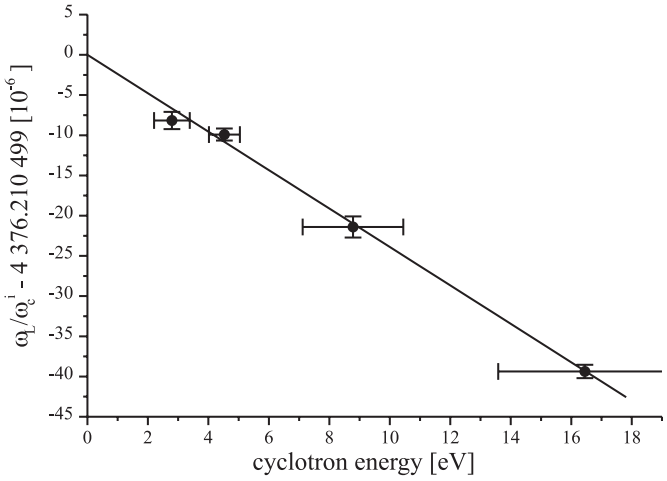

Fig. 29. Extrapolation of (ω_L/ω_c) to zero cyclotron energy. The shift $\Delta(\omega_L/\omega_c)$ is $-2.3\times10^{-6}E_+/\mathrm{eV}$. This corresponds to a relative change of the frequency ratio of $-1.07\times10^{-9}E_+/\mathrm{eV}$.

From the shifts of the cyclotron and Larmor frequencies we obtain a shifted value for ω_L/ω_c, $(\omega_L/\omega_c)_s$:

$$\begin{aligned}\Delta(\omega_L/\omega_c)_s &\approx \frac{\partial(\omega_L/\omega_c)_s}{\partial\omega_L}\Delta\omega_L + \frac{\partial(\omega_L/\omega_c)_s}{\partial\omega_c}\Delta\omega_c \\ &= \frac{(\omega_L/\omega_c)_s}{\omega_L}\Delta\omega_L - \frac{(\omega_L/\omega_c)_s}{\omega_c}\Delta\omega_c \\ &= -(\omega_L/\omega_c)_s\frac{\omega_z}{\omega_+^2}\,\Delta\omega_z. \end{aligned} \quad (44)$$

We obtain the final value for ω_L/ω_c from an extrapolation of the measured $(\omega_L/\omega_c)_s$ to vanishing cyclotron energy (Fig. 29). In order to perform the extrapolation, we grouped the events (ratios ω_{mw}/ω_c) according to the cyclotron energy at which they happened, into 4–6 bins. The plot in Figure 29 shows the result when the data is grouped into 4 bins. According to equations (42) and (14), we extrapolate linearly to zero energy. The average slope of the fits to 4, 5, and 6 bins is

$$\Delta(\omega_L/\omega_c) = -2.3\,(3)\times10^6E_+/\mathrm{eV}. \quad (45)$$

The uncertainty here is given by the average uncertainty of each fit. This slope is consistent with equations (43) and (44).

As ω_L/ω_c for vanishing cyclotron energy, we took the average of the extrapolations for 4, 5, and 6 cyclotron energy bins. The result is

$$\omega_L/\omega_c = 4376.210\,500\,2\,(18). \quad (46)$$

The number in parentheses is the mean of the fitting uncertainties.

4.3 Magnetic field fluctuations

Temporal fluctuations of the magnetic field can be a severe limitation to the attainable precision. We observe drifts and fluctuations of the B-field that are typically of the order of 10^{-8} during the time interval of one measurement cycle (20–30 min). In addition, the magnetic field shows big jumps of about 10^{-7} when either liquid nitrogen or helium is filled into the apparatus. Mechanical stress and changes in the temperature of the baths change the trap position. Movements of the nickel ring induce currents in the superconducting coils of the magnet and thus change the magnetic field. In our case the stability of the magnetic field is of little importance at our level of accuracy because we measure the cyclotron and Larmor frequencies at the same time and field fluctuations cancel to first order. We have therefore not yet taken any measures to stabilize the magnetic field [39,40].

4.4 Electric field

Uncertainties in the measured ratio ω_L/ω_c also arise from imperfections of the electric field. Anharmonicities in the trapping potential shift the axial frequency when the axial temperature of the ion is raised by excitation (Sect. 3.1.2, Fig. 15). This technique was used to accelerate the axial frequency measurements both in the precision and in the analysis trap. For the critical determination of the axial frequency in the precision trap, we increase the ion's axial energy by a factor of 9, corresponding to an axial temperature of 500 K. By adjusting the tuning ratio (Sect. 3.1.4) we can reduce the octupole contribution (C_4) to less than 10^{-5}. This corresponds to a maximum relative uncertainty in the axial frequency measurement of 50 mHz and in ω_L/ω_c of 1×10^{-10}. Another imperfection would be a tilt of the trapping potential axis *versus* the magnetic field and a breaking of the axial symmetry (ellipticity). In equation (21), these imperfection do not enter in first order [24].

4.5 Image charge

The interaction of a trapped charged particle with the induced image charges was investigated with respect to the

electron $g-2$ experiment on free electrons by Fischbach *et al.* in reference [41] and by Boulware *et al.* in reference [42]. They conclude that the shift in the cyclotron frequency of the electron due to the retardation of the interaction is proportional to the classical electron radius $r_e = e^2/2\pi m_e c^2$ and inversely proportional to the distance to the electrodes. These shifts have been estimated in case of the $g-2$ experiment [41,42] to amount to less than 10^{-12}. Replacing e and m_e by the charge and mass of hydrogen-like carbon, we conclude that in our case this shift is smaller by a factor of 50 and is therefore negligible. An intuitive argument for this fact is that the wavelength for excitation of the ion's cyclotron motion is 12 m, much larger than the trap-cavity size.

This argument, however, is only valid for the electric field component perpendicular to the direction from the ion to the electrode surfaces. As shown both experimentally and theoretically by van Dyck *et al.* [43], the longitudinal part of the self-induced electric field can shift the eigenfrequencies of ions substantially. They modeled their hyperbolic trap by a spherical cavity. Recently Porto [44] calculated the image charge shifts for arbitrary axially symmetric cavities.

The Coulomb force in the cylindrical trap between the ion (at rest) and the induced image charge in our cylindrical trap of radius r_0 is

$$\mathbf{F}(r) = \frac{q^2\, r_0/r}{4\pi\epsilon_0 |r - r_0^2/r|^2}\hat{\mathbf{e}}_r \approx \frac{q^2}{4\pi\epsilon_0 r_0^3}\mathbf{r}. \tag{47}$$

In the plane perpendicular to the z-axis this is the same force as obtained from the spherical model [43]. There is, however, no force at all in the z-direction because our trap is translationally invariant along the z-axis (the boundaries of the cavity in this direction are far away compared to the radius of the cavity). Therefore the axial frequency is not affected at all by the image-charge interaction. For the motions in the radial plane, the attractive force increases the magnetron frequency by

$$\Delta\omega_- \approx \frac{\omega_{z,\mathrm{v}}^2}{2\omega_\mathrm{c}} - \frac{\omega_z^2}{2\omega_\mathrm{c}} = +\frac{q^2}{4\pi\epsilon_0 m r_0^3\,\omega_\mathrm{c}}\,. \tag{48}$$

For the perturbed cyclotron frequency we obtain a reduction,

$$\Delta\omega_+ \approx \left[\omega_\mathrm{c} - \frac{\omega_{z,\mathrm{v}}^2}{2\omega_\mathrm{c}}\right] - \left[\omega_\mathrm{c} - \frac{\omega_z^2}{2\omega_\mathrm{c}}\right] \approx -\frac{q^2}{4\pi\epsilon_0 m r_0^3\,\omega_\mathrm{c}}\,. \tag{49}$$

From equation (21), for the unperturbed cyclotron frequency we have

$$\frac{\Delta\omega_\mathrm{c}}{\omega_\mathrm{c}} = \left(-\frac{\omega_+}{\omega_\mathrm{c}} + \frac{\omega_-}{\omega_\mathrm{c}}\right)\frac{q^2}{4\pi\epsilon_0 m\, r_0^3\,\omega_\mathrm{c}^2}\,. \tag{50}$$

This shifts the cyclotron frequency downwards by $2.92\ (24) \times 10^{-10}$ in our case. The error is deduced by assuming a maximum motional cyclotron amplitude of 100 μm of the ion, which introduces a corresponding variation in the distance r_0 between the ion and the trap electrodes.

4.6 Special relativity

At the level of 10^{-9}, to which we measure our frequencies, we may have to account for relativistic effects in spite of the low motional energies. The following discussion, however, will show that they can be neglected for the $(\omega_\mathrm{L}/\omega_\mathrm{c})$ resonance, because the Larmor and cyclotron frequencies are shifted by almost the same amount. Relativistically, the cyclotron frequency can be written

$$\omega_\mathrm{c}(\gamma) = \frac{q}{\gamma m}B_z = \frac{1}{\gamma}\omega_\mathrm{c}(\gamma = 1). \tag{51}$$

Here

$$\gamma = 1/\sqrt{1 - v^2/c^2} \tag{52}$$

describes the change of the magnetic field due to the coordinate transformation into the center-of-mass system of the ion. This is a pure electrodynamic effect. The transformation of the Larmor precision frequency ω_L is more complicated. We follow Mendlowitz and Case [45] (see also Refs. [46,47]) and distinguish two cases.

1. Motion parallel to the magnetic field:

$$\omega_\mathrm{L}(\gamma) = (1+a)\omega_\mathrm{c}^e(\gamma) = \frac{1}{\gamma}\omega_\mathrm{L}(\gamma = 1). \tag{53}$$

   Here $a = g/2 - 1$ denotes the anomaly of the magnetic moment of the electron. Comparison with equation (51) shows that the axial motion of the ion shifts both the Larmor precession and the cyclotron frequency by the same amount. Therefore the ratio does not depend on the axial energy.

2. Motion perpendicular to the magnetic field:

$$\begin{aligned}\omega_\mathrm{L}(\gamma) &= (1+\gamma a)\omega_\mathrm{c}^e(\gamma)\\ &= \frac{1}{\gamma}\omega_\mathrm{L}(\gamma = 1) + \left(1 - \frac{1}{\gamma}\right)a\omega_\mathrm{L}(\gamma = 1)\\ &= \frac{1}{\gamma}\omega_\mathrm{L}(\gamma = 1) + \frac{v^2}{2c^2}a\omega_\mathrm{L}(\gamma = 1).\end{aligned} \tag{54}$$

   Comparison with equation (51) shows that here the transformation behaviour is different for both frequencies. The anomaly a is about 10^{-3} and therefore the difference in the transformation behaviour is small.

During the measurement, the ion's cyclotron energy is raised to about 1–5 eV. The corresponding relativistic corrections of $\omega_\mathrm{L}/\omega_\mathrm{c}$ are of the order of 10^{-12} and are therefore negligible.

4.7 Other systematic uncertainties

Here we briefly consider other possible sources of systematic errors.

– **Finite magnetron motion**
  Similar to the cyclotron motion, there is also a magnetic moment associated with the magnetron motion. In an inhomogeneous magnetic field, the corresponding additional force gives rise to modifications

of equation (9). But due to the low frequency, the resulting magnetic moment is very small. Since the magnetron radius is of the same order as the cyclotron radius (see Tab. 2) is orbital magnetic moment is smaller by the ratio of frequencies (10^{-3}). From the measured dependence an the cyclotron energy we calculate the relative corrections to $\omega_{\rm L}/\omega_{\rm c}$ to less 10^{-11} for the magnetron motion.

– **Microwave field**
Inside of our cavity, the microwave field forms a standing wave with a periodicity of 1.5 mm. Since the ion amplitudes are in the range of 100 μm, the intensity varies by about 3%. This causes a slightly higher spin-flip probability at positions of high microwave intensity. Together with the magnetic field gradient of 60 μT/mm (corresponding to relative gradient of 1.5×10^{-6}) this would lead to a systematic shift for $\omega_{\rm L}/\omega_{\rm c}$ of $0.03 \times 1.5 \times 10^{-6} \approx 5 \times 10^{-8}$. However, the spin-flip rate is much smaller than the oscillation frequencies so that the spin flips occur on a time scale long compared to the oscillation periods and thus the effect of the inhomogeneous microwave field is strongly reduced. Because of the geometry of the microwave field, we would expect the largest effect from the axial motion, which can be estimated to be less than 10^{-14}, assuming a coherence time of 1 s (which actually might even be substantially longer and thus reducing the effect even more).

– **Quartz oscillators**
For the experiment, all synthesizers were locked in a chain to a 10 MHz signal of an atomic clock. However, it was not possible to lock our Fast-Fourier-transform (FFT) analyzer which measures the cyclotron frequency mixed down from 24 MHz to 1.5 kHz. Therefore we corrected the FFT data for the measured deviation of its oscillator from the clock signal. Assuming a (moderate) stability of 2×10^{-6} of the FFT oscillator we obtain a final relative contribution of 1×10^{-10} to the uncertainty in $\omega_{\rm L}/\omega_{\rm c}$.

– **Grounding**
A small correction also arises from an observed change in the grounding potential when we measure the axial and the cyclotron frequency. The change of the ground of about 1 μV is induced by control commands sent by the computer over the GPIB-interface. The axial frequency is shifted during its measurement by about 50 mHz as compared to its value while the cyclotron frequency measurement takes place. The fractional shift for $\omega_{\rm c}$ from equation (21) and corresponding for $\omega_{\rm L}/\omega_{\rm c}$ is 7×10^{-11}. The uncertainty is conservatively estimated to 4×10^{-4}. This leads to a fractional shift of 7×10^{-11} for $\omega_{\rm c}$ in and therefore also for $\omega_{\rm L}/\omega_{\rm c}$.

5 Final result

The quantity measured in our experiment is the ratio of the Larmor frequency of the electron bound in $^{12}C^{5+}$ and the cyclotron frequency of the $^{12}C^{5+}$-ion. The result after all corrections (Tab. 4) and extrapolations (Sects. 4.2 and 4.1.2) is

$$\omega_{\rm L}/\omega_{\rm c}(C^{5+}) = 4\,376.210\,498\,9\ (19)\ (13). \qquad (55)$$

The first number in parentheses refers to the statistical uncertainty resulting from the extrapolations and the second one represents the quadratically summed systematic uncertainties (see Tab. 3).

Applying the ratio of cyclotron frequencies for the electron and $^{12}C^{5+}$ (Eq. (5)) derived from measurements by van Dyck *et al.* [17,18] ($6m_e/M_{^{12}C^{6+}} = 0.000\,274\,365\,185\,89$) (58) and using equation (4), we obtain the g_J factor of the electron bound in $^{12}C^{5+}$

$$g(C^{5+}) = 2.001\,041\,596\ (5). \qquad (56)$$

This is the most precise determination of any atomic magnetic moment so far. It also accurately quantifies for the first time experimentally the effects of bound-state QED on a magnetic moment. Our result is in good agreement with the theoretical calculations from the groups in St. Petersburg [15,48] and Göteborg [2,49] and verifies the bound-state-QED contributions to about 1%. As was shown in [14], it even allows for an independent determination of the mass of the electron.

Future prospects

Currently the accuracy to which $\omega_{\rm L}/\omega_{\rm c}$ can be determined is limited mainly by magnetic field inhomogeneities. They lead both to systematic and statistical uncertainties. The main part of the systematic uncertainty is the asymmetry in the lineshape (Sect. 4.1.2) and the energy dependence of the cyclotron frequency (Sect. 4.2). The statistical uncertainty is mainly determined by the number of observed spin flips and the width of the line. All of the uncertainties caused by the magnetic inhomogeneity add to the most significant contributions of the total error budget. Therefore we plan to improve the spatial homogeneity by tuning the currents in the shim coils of the magnet. The tuning can be monitored by the methods described in Section 4.1.3. It should be possible to reduce the quadratic part of the B-field, characterized by B_2, by about a factor of 10 compared to its present value. As a consequence, the resonance would be narrower and the remaining asymmetry would be smaller. Recently we have stabilized the helium pressures in the magnet and apparatus dewars. The constant pressure reduces temperature fluctuations in the coil material and thus leads to a more stable flux density of the magnetic field [40,50].

It is of equal importance to reduce the axial temperature from 60 K to that of the environment at 4 K. The corresponding reduction in motional amplitude would lead to a smaller linewidth, too. It is, however, difficult to locate the source of additional noise since our electronic circuits are not accessible while operating at 4 K.

After improving the homogeneity of the magnetic field, the remaining statistical uncertainty would be dominated

by axial-frequency fluctuations. Here the limitation is not the statistical noise in the measurement signal, but the electric field fluctuations in the μV-range. These could be reduced by improving the stability of our voltage source.

We point out that our method to determine the g factor of the bound electron can be applied to almost any atomic system without reduction in the expected accuracy provided masses are known well enough. For hydrogen like ions with higher nuclear charge the axial frequency change connected with a spin-flip will be smaller. This has to be compensated by a larger magnetic field inhomogeneity in the analysis trap to make this change observable [51]. Even measurements of the proton and of nuclear magnetic moments are imaginable [52]. Extension of our measurements to other ions requires a precise knowledge of their atomic masses (or the ratio of the electron and the ion cyclotron frequencies). For many ions such accurate mass measurements ($\Delta m/m \sim 10^{-10}$) have already been carried out [17,53,54] and thus are a promising base for future experiments at our setup.

We are grateful to G. Soff, V.A. Yerokhin, V.M. Shabaev, V. Natarajan, S. Peil, and J.V. Porto, for many stimulating and helpful discussions. Financial support was obtained from the European Union under the contract numbers ERB FMRX CT 97-0144 (EUROTRAPS project) and HPRI-CT-2001-5036 (HITRAP project).

References

1. W. Quint, Phys. Scripta **T59**, 203 (1995)
2. T. Beier *et al.*, Phys. Rev. A **62**, 032510 (2000)
3. H. Häffner *et al.*, Phys. Rev. Lett. **85**, 5308 (2000)
4. P. Mohr, G. Plunien, G. Soff, Phys. Rep. **293**, 227 (1998)
5. T. Beier, Phys. Rep. **339**, 79 (2000)
6. V.M. Shabaev *et al.*, Phys. Rev. Lett. **86**, 3959 (2001)
7. L.C. Balling, F.M. Pipkin, Phys. Rev. **139**, A19 (1965)
8. F.G. Walther, W.D. Phillips, D. Kleppner, Phys. Rev. Lett. **28**, 1159 (1972)
9. J.S. Tiedeman, H.G. Robinson, Phys. Rev. Lett. **39**, 602 (1977)
10. C.E. Johnson, H.G. Robinson, Phys. Rev. Lett. **45**, 250 (1980)
11. P. Seelig *et al.*, Phys. Rev. Lett. **81**, 4824 (1998)
12. H. Winter *et al.*, GSI Scientific Report 1998, p. 87, 1999
13. V.M. Shabaev, Can. J. Phys. **76**, 907 (1998)
14. T. Beier *et al.*, Phys. Rev. Lett. **88**, 011603 (2002)
15. V.A. Yerokhin, P. Indelicato, V.M. Shabaev, Phys. Rev. Lett. **89**, 143001 (2002)
16. P.J. Mohr, B.N. Taylor, Rev. Mod. Phys. **72**, 351 (2000)
17. R.S. van Dyck Jr, D.L. Farnham, P.B. Schwinberg, Phys. Scripta **T59**, 134 (1995)
18. D.L. Farnham, R.S. van Dyck Jr, P.B. Schwinberg, Phys. Rev. Lett. **75**, 3598 (1995)
19. N. Hermanspahn *et al.*, Phys. Rev. Lett. **84**, 427 (2000)
20. M. Diederich *et al.*, Hyper. Interact. **115**, 185 (1998)
21. G. Gabrielse, L. Haarsma, S.L. Rolston, Int. J. Mass Spectrom. Ion Process. **88**, 319 (1989)
22. R.E. Olson, A. Salop, Phys. Rev. A **14**, 579 (1976)
23. S. Stahl, Ph.D. thesis, University of Mainz, Germany, 1998
24. L.S. Brown, G. Gabrielse, Rev. Mod. Phys. **58**, 233 (1986)
25. L.S. Brown, G. Gabrielse, Phys. Rev. A **25**, 2423 (1982)
26. D.J. Wineland, H.G. Dehmelt, J. Appl. Phys. **46**, 919 (1975)
27. E.A. Cornell, R.M. Weisskoff, K.R. Boyce, D.E. Pritchard, Phys. Rev. A **41**, 312 (1990)
28. M. Kretzschmar, in *Trapped Charged Particles and Fundamental Physics*, edited by D. Dubin, D. Schneider, AIP Conf. Proc. **457**, 242 (1999)
29. R.S. van Dyck Jr, P.B. Schwinberg, H.G. Dehmelt, Phys. Rev. Lett. **59**, 26 (1987).
30. H. Dehmelt, P. Ekstrom, Bull. Am. Phys. Soc. **18**, 727 (1973).
31. L.S. Brown, Phys. Rev. Lett. **52**, 2013 (1984)
32. L.S. Brown, Ann. Phys. (NY) **159**, 62 (1985)
33. N. Bloembergen, E.M. Purcell, R.V. Pound, Phys. Rev. **73**, 679 (1948)
34. S.F. Watanabe, H.G. Robinson, J. Phys. B: At. Mol. Phys. **10**, 931 (1977)
35. D. Brenner, Phys. Rev. **185**, 26 (1969)
36. M. Kretzschmar, Z. Naturf. **45a**, 965 (1990)
37. Ch. Gerz, D. Wilsdorf, G. Werth, Nucl. Instr. Meth. B **47**, 453 (1990)
38. G. Bollen, R.B. Moore, G. Savard, H. Stolzenberg, J. Appl. Phys. **68**, 4355 (1990)
39. R.S. van Dyck Jr, D.L. Farnham, S.L. Zafonte, P.B. Schwinberg, in *Trapped Charged Particles and Fundamental Physics*, edited by D. Dubin, D. Schneider, AIP Conf. Proc. **457**, 101 (1999)
40. R.S. van Dyck Jr, D.L. Farnham, S.L. Zafonte, P.B. Schwinberg, Rev. Sci. Instr. **70**, 1665 (1999)
41. E. Fischbach, N. Nakagawa, Phys. Rev. D **30**, 2356 (1984)
42. D.G. Boulware, L.S. Brown, T. Lee, Phys. Rev. D **32**, 729 (1985)
43. R.S. van Dyck Jr, F.L. Moore, D.L. Farnham, P.B. Schwinberg, Phys. Rev. A **40**, 6308 (1989)
44. J.V. Porto, Phys. Rev. A **64**, 023403 (2001)
45. H. Mendlowitz, K.M. Case, Phys. Rev. **97**, 33 (1955)
46. F. Combley, F.J.M. Farley, J.H. Field, E. Picasso, Phys. Rev. Lett. **42**, 1383 (1979)
47. V. Bargmann, L. Michel, V.L. Telegdi, Phys. Rev. Lett. **2**, 435 (1958)
48. V.M. Shabaev, V.A. Yerokhin, Phys. Rev. Lett. **88**, 091801 (2002)
49. H. Persson, S. Salomonson, P. Sunnergren, I. Lindgren, Phys. Rev. A **56**, R2499 (1997)
50. G. Gabrielse, J. Tan, J. Appl. Phys. **63**, 5143 (1988)
51. G. Werth, H. Häffner, W. Quint, Adv. At. Mol. Opt. Phys. **48**, 191 (2002)
52. G. Werth *et al.*, *The g_J Factor of Hydrogenic Ions: A Test of Bound State QED*, The hydrogen Atom: Precision Physics of Simple Atomic Systems, edited by S.G. Karshenboim, F.S. Pavone, G.F. Bassani, M. Inguscio, T.W. Hänsch (Springer-Verlag, 2001)
53. F. DiFilippo, V. Natarajan, K.R. Boyce, D.E. Pritchard, Phys. Rev. Lett. **73**, 1481 (1994)
54. M.P. Bradley, J.V. Porto, S. Rainville, J.K. Thompson, D.E. Pritchard Phys. Rev. Lett. **83**, 4510 (1999)